JOURNAL OF GEOPHYSICAL RESEARCH: SOLID EARTH, VOL. 118, 2586–2617, doi:10.1002/jgrb.50124, 2013

3-D multiobservable probabilistic inversion for the compositional and thermal structure of the lithosphere and upper mantle. I: *a priori* petrological information and geophysical observables

J. C. Afonso,[1] J. Fullea,[2,3] W. L. Griffin,[1] Y. Yang,[1] A. G. Jones,[2] J. A. D. Connolly,[4] and S. Y. O'Reilly[1]

Received 14 June 2012; revised 4 February 2013; accepted 6 February 2013; published 30 May 2013.

[1] Traditional inversion techniques applied to the problem of characterizing the thermal and compositional structure of the upper mantle are not well suited to deal with the nonlinearity of the problem, the trade-off between temperature and compositional effects on wave velocities, the nonuniqueness of the compositional space, and the dissimilar sensitivities of physical parameters to temperature and composition. Probabilistic inversions, on the other hand, offer a powerful formalism to cope with all these difficulties, while allowing for an adequate treatment of the intrinsic uncertainties associated with both data and physical theories. This paper presents a detailed analysis of the two most important elements controlling the outputs of probabilistic (Bayesian) inversions for temperature and composition of the Earth's mantle, namely the *a priori* information on model parameters, $\rho(m)$, and the likelihood function, $L(m)$. The former is mainly controlled by our current understanding of lithosphere and mantle composition, while the latter conveys information on the observed data, their uncertainties, and the physical theories used to relate model parameters to observed data.

[2] The benefits of combining specific geophysical datasets (Rayleigh and Love dispersion curves, body wave tomography, magnetotelluric, geothermal, petrological, gravity, elevation, and geoid), and their effects on $L(m)$, are demonstrated by analyzing their individual and combined sensitivities to composition and temperature as well as their observational uncertainties. The dependence of bulk density, electrical conductivity, and seismic velocities to major-element composition is systematically explored using Monte Carlo simulations. We show that the dominant source of uncertainty in the identification of compositional anomalies within the lithosphere is the intrinsic nonuniqueness in compositional space. A general strategy for defining $\rho(m)$ is proposed based on statistical analyses of a large database of natural mantle samples collected from different tectonic settings (xenoliths, abyssal peridotites, ophiolite samples, etc.). This strategy relaxes more typical and restrictive assumptions such as the use of local/limited xenolith data or compositional regionalizations based on age-composition relations. We demonstrate that the combination of our $\rho(m)$ with a $L(m)$ that exploits the differential sensitivities of specific geophysical observables provides a general and robust inference platform to address the thermochemical structure of the lithosphere and sublithospheric upper mantle. An accompanying paper deals with the integration of these two functions into a general 3-D multiobservable Bayesian inversion method and its computational implementation.

Citation: Afonso, J. C., J. Fullea, W. L. Griffin, Y. Yang, A. G. Jones, J. A. D. Connolly, and S. Y. O'Reilly (2013), 3-D multi-observable probabilistic inversion for the compositional and thermal structure of the lithosphere and upper mantle. I: *a priori* petrological information and geophysical observables, *J. Geophys. Res. Solid Earth*, *118*, 2586–2617, doi:10.1002/jgrb.50124.

Additional supporting information may be found in the online version of this article.

Corresponding author: J. C. Afonso, Australian Research Council Centre of Excellence for Core to Crust Fluid Systems/GEMOC, Department of Earth and Planetary Sciences, Macquarie University, Sydney, Australia. (juan.afonso@mq.edu.au)

2169-9313/13/10.1002/jgrb.50124

[1]Australian Research Council Centre of Excellence for Core to Crust Fluid Systems/GEMOC, Department of Earth and Planetary Sciences, Macquarie University, Sydney, Australia.
[2]Dublin Institute for Advanced Studies, 5 Merrion Square, Dublin, Ireland.
[3]Institute of Geosciences (IGEO) CSIC-UCM José Antonio Novais, 2, 28040, Madrid, Spain.
[4]Institute of Geochemistry and Petrology, ETH Zurich, Switzerland.

1. Introduction

[3] The conversion of geophysical observables [e.g., travel time curves, gravity anomalies, surface heat flow (SHF)] into robust estimates of the true thermochemical structure of the Earth's interior is one of the most fundamental goals of the Geosciences. It is the physical state of the deep rocks that drives processes such as volcanism, seismic activity, and tectonism. Detailed knowledge of the thermal and compositional structure of the upper mantle is an essential requirement for understanding the formation, deformation, and destruction of continents, the physical and chemical interactions between the lithosphere and the convecting sublithospheric mantle, the long-term stability of ancient lithosphere, and the development and evolution of surface topography.

[4] Inferring physical parameters such as wave velocities, density, or electrical conductivity, within the Earth is informative but not particularly useful if they are not converted into information about the Earth's thermochemical structure. Ultimately, the ability to perform such conversions not only determines our understanding of the Earth's interior but also has the potential to directly inform about the location of mineral and energy resources.

[5] Current knowledge of the thermal and compositional structure of the lithosphere and the sublithospheric mantle essentially derives from four independent sources.

[6] (i) The most widely applied modeling approach uses gravity and/or SHF data to obtain a model of the temperature and/or density structure of the lithosphere that fits the data to some acceptable level [e.g., *Zeyen and Fernàndez*, 1994; *Zeyen et al.*, 2005; *Ebbing et al.*, 2006; *Jiménez-Munt et al.*, 2008; *Chappell and Kusznir*, 2008; *Kaban et al.*, 2010]. Typically, the density of the mantle is treated as constant or T-dependent only. More sophisticated variants integrate concepts from thermodynamics, mineral physics, heat transfer, and/or isostatic modeling to derive lithospheric/sublithospheric models that simultaneously fit two or more constraining datasets [e.g., *Sobolev et al.*, 1997; *Khan et al.*, 2007; *Afonso et al.*, 2008; *Fernàndez et al.*, 2010; *Fullea et al.*, 2009, 2010, 2011; *Simmons et al.*, 2009; *Kuskov et al.*, 2011].

[7] (ii) The second most common approach applied to the lithosphere and upper mantle is based on the modeling of seismic data. The aim here is to test thermal and mineralogical (or density) models that are compatible with seismic data (usually shear waves) by using either thermodynamic concepts and/or experimental data from mineral physics [e.g., *Bass and Anderson*, 1984; *Shapiro and Ritzwoller*, ; *Ritzwoller et al.*, 2004; *Priestley and McKenzie*, 2006; *Ritsema et al.*, 2009; *Cammarano et al.*, 2011]. Typically, these studies do not invert directly for composition but rather assume *a priori* "representative" compositional models. These are then used to generate synthetic data that can be compared with some seismological observation to test whether or not the model is consistent with the observation.

[8] (iii) The third source of independent information is provided by models and data derived from magnetotellurics (MT). MT is a natural-source electromagnetic method based on the relationship between the temporal variations of electric and magnetic fields at the Earth's surface and its subsurface electrical structure [cf. *Jones*, 1999]; the latter is the output of an MT model. Since the electrical conductivity of solid aggregates is exponentially sensitive to temperature through an Arrhenius relationship, MT has the potential to provide relatively tight constraints on temperature in the lithosphere. Recent studies have shown encouraging results towards linking conductivity, composition, temperature, and seismic velocities through petrophysical parameters [e.g., *Xu et al.*, 2000; *Khan et al.*, 2006; *Jones et al.*, 2009; *Fullea et al.*, 2011 and references therein].

[9] (iv) Finally, the only direct approach is the petrological-geochemical estimation of thermobarometric and chemical data from xenoliths (fragments of upper mantle brought up to the surface by volcanism) and exhumed mantle sections. Where specific mineral assemblages (typically olivine + orthopyroxene ± clinopyroxene ± garnet) are present, xenoliths can be used to derive the compositional and paleo-thermal structure beneath specific localities [e.g., *Griffin et al.*, 1984; *O'Reilly and Griffin*, 1996, 2006; *Kukkonen and Peltonen*, 1999; *James et al.*, 2004]. Unfortunately, the spatial and temporal coverage provided by this method is limited, and the extrapolations and interpolations needed to model large sections of the mantle carry unquantifiable uncertainties (see below). Also, the bulk composition of specific xenolith suites may have been affected by the exhumation process [cf. *O'Reilly and Griffin*, 2012], and therefore, the question of whether they provide a representative picture of the mantle they sampled is raised.

[10] At present, there are often significant discrepancies between the predictions from these four approaches [cf. *O'Reilly et al.*, 2010]. Indeed, different research groups have recently proposed mutually incompatible models of the lithosphere while using similar input data and/or methods [e.g., *Priestley and McKenzie*, 2006; *Deen et al.*, 2006; *Li et al.*, 2008; *Fishwick*, 2010; *Becker*, 2012]. In particular, given the trade-offs between temperature and composition, seismic wave velocities alone are not sufficient to tightly constrain the thermal and compositional structures of the upper mantle [e.g., *Trampert et al.*, 2004; *Afonso et al.*, 2010]. Moreover, as we show here, many different ultramafic rocks (i.e., compositions) can produce the same seismic response, so nonuniqueness is inherent. Uncertainties associated with traditional seismic tomography methods, anisotropy, anelasticity, and geotherm estimations further complicate the task. All this leads to a lack of confidence in our knowledge of some important features of the Earth's lithosphere and upper mantle [e.g., the lithosphere-asthenosphere boundary (LAB)].

[11] One strategy for obtaining more consistent and robust models, and at the same time understanding the root causes of the discrepancies between the different methods (an important problem in itself), is to simultaneously fit all the available geophysical and petrological observables using an internally consistent approach in which all observables and model parameters are related through a unique and robust physical theory. In principle, such a scheme would reduce the uncertainties associated with the modeling of individual observables and could distinguish between thermal or compositional variations at different depths, since different observables respond differently to shallow/deep, thermal/compositional anomalies.

[12] Such an integrated modeling approach has been proposed recently within a forward, user-guided scheme [*Afonso et al.*, 2008; *Fullea et al.*, 2009]. This method has two critical advantages over traditional inversion schemes: (i) the model can be made as complicated (i.e., realistic) as needed, given modest computational power, and (ii) modeler's experience (i.e., "human intuition") is maximized during the modeling process instead of relying purely on a fixed set of algorithms. However, the forward approach also has three important drawbacks: (i) it requires continuous (time-consuming) input from the modeler as well as a high level of expertise, (ii) uncertainties and the uniqueness of the model are practically impossible to quantify, and (iii) erroneous preconceptions from the modeler can negatively affect the reliability of the model to a large extent.

[13] Inversion schemes, on the other hand, deal objectively with data and overcome most of the above limitations. Unfortunately, traditional (nonprobabilistic) inversion methods used to make inferences about the thermochemical structure of the Earth's mantle are not well suited to deal with one or more of the following problems:

[14] (1) Strong nonlinearity of the system. Traditional linearized inversions do not generally provide reliable estimates.

[15] (2) The temperature effect on geophysical observables is in most cases greater than the compositional effect; therefore, the latter is more difficult to isolate.

[16] (3) Nonuniqueness of the compositional field. Different compositions can fit equally well seismic and potential field observations.

[17] (4) Intrinsic correlations between physical parameters (e.g., shear and compressional velocities) and/or between geophysical observables (e.g., dispersion data and apparent resistivity) are commonly ignored or modeled with simple empirical equations (e.g., Birch's law) that do not necessarily have general applicability.

[18] (5) Trade-off between temperature and composition in wave speeds.

[19] The nonlinear thermodynamically self-consistent method of *Khan et al.* [2011a, 2011b] is a relevant exception. Their Bayesian method is truly nonlinear and inverts directly for composition and temperature. However, although it represents one of the most advanced and well-suited methods available, it has been applied only to low-resolution tomographic problems (5° × 5° spacing) within a limited compositional space.

[20] In this work, we present a new nonlinear, 3-D, multiobservable probabilistic inversion approach specifically designed to circumvent/minimize the abovementioned problems. The method uses a probabilistic (Bayesian) inference approach as the general framework to solve the inverse problem. In the past 20 years, Bayesian methods applied to inverse problems have become standard and powerful tools in geophysics, and many review papers and textbooks are now available on the subject [cf. *Mosegaard*, 1998; *Bosch*, 1999; *Mosegaard and Tarantola*, 2002; *Mosegaard and Sambridge*, 2002; *Tarantola*, 2005; *Idier*, 2008; *Biegler et al.*, 2011]. Within this probabilistic framework, the objective is to assign representative probabilities to competing hypotheses by combining information from observed data (measurements), physical theories, and any prior information we may have about the problem at hand.

1.1. Summary of Bayesian Inversion

[21] In geophysics, we typically deal with a (continuous or discontinuous) hypothesis space characterized by the entire set of parameters defining "acceptable Earth models," that is, models that reproduce or explain certain observed/measured data to some "acceptable" degree. In this context, the most general solution to these kinds of inversion problems is represented by a probability density function (PDF) known as the **posterior** PDF. This PDF contains all current information about the problem at hand, and it can be thought of as an objective measure of our best state of knowledge on the problem. Formally, this posterior PDF can be written as [cf. *Tarantola*, 2005]

$$\sigma(\mathbf{d},\mathbf{m}) = k\,\frac{\rho(\mathbf{d},\mathbf{m})\,\Theta(\mathbf{d},\mathbf{m})}{\mu(\mathbf{d},\mathbf{m})} \tag{1}$$

where $\sigma(\mathbf{d},\mathbf{m})$ is the posterior PDF (strictly, a joint PDF in the parameter and data space), k a normalization constant, $\rho(\mathbf{d},\mathbf{m})$ the joint prior PDF describing all *a priori* information in the data and parameter space, $\Theta(\mathbf{d},\mathbf{m})$ a joint PDF describing the correlations and uncertainties of a particular physical theory connecting model parameters and predicted data, $\mu(\mathbf{d},\mathbf{m})$ the homogenous joint PDF (constant in Cartesian spaces), $\mathbf{m}$ the vector of model parameters, and $\mathbf{d}$ the vector containing the observable data. The posterior PDF so defined contains all available information on both observable data and *a priori* information on model parameters. Importantly, integrating out the data vector component from $\sigma(\mathbf{d},\mathbf{m})$ gives the marginal PDF in the model space as

$$\sigma(\mathbf{m}) = \int \sigma(\mathbf{d},\mathbf{m})\,\mathrm{d}\mathbf{d} \tag{2}$$

[22] The latter gives the probability of all possible combinations of model parameters allowed for the vector $\mathbf{m}$, and therefore, it constitutes the solution to the inversion problem. Under most circumstances, applying standard rules of probability theory allows us to define [cf. *Tarantola*, 2005]

$$\Theta(\mathbf{d},\mathbf{m}) = \theta(\mathbf{d}\mid\mathbf{m})\,\mu(\mathbf{m}) \tag{3}$$

$$\rho(\mathbf{d},\mathbf{m}) = \rho(\mathbf{m})\,\rho(\mathbf{d}) \tag{4}$$

$$\mu(\mathbf{d},\mathbf{m}) = \mu(\mathbf{m})\,\mu(\mathbf{d}) \tag{5}$$

where $\theta(\mathbf{d}\,|\,\mathbf{m})$ is the PDF for $\mathbf{d}$ conditional on $\mathbf{m}$. This PDF plays the role of assigning uncertainties to the predictions from the physical theories used to model the data (*forward problem*). Using equations (1)–(5), we can write

$$\sigma(\mathbf{m}) = k\,\rho(\mathbf{m})\,L(\mathbf{m}) \tag{6}$$

$$L(\mathbf{m}) = \int \frac{\rho(\mathbf{d})\,\theta(\mathbf{d}\mid\mathbf{m})}{\mu(\mathbf{d})}\,\mathrm{d}\mathbf{d} \tag{7}$$

where $\rho(\mathbf{m})$ is the prior PDF describing our *a priori* knowledge (or prejudice) on the model parameters and $L(\mathbf{m})$ is the so-called *likelihood function*, which measures how well a particular model explains the data. Clearly, $\sigma(\mathbf{m})$ is controlled by the respective forms of $\rho(\mathbf{m})$ and $L(\mathbf{m})$, and thus, particular care needs to be taken in defining/evaluating these functions. For example, assume that we have a system with

only one model parameter m_0; if the observed data $d(m_0)$ are extremely sensitive to variations of this target parameter, and our physical theory describing the problem is exact, then the likelihood function $L(m_0)$ will have a very narrow peak about the true value of m_0, and so will $\sigma(m_0)$ (Figures 1a and 1b). In this case, the true value of m_0 is easily recovered (with high probability), regardless of the poor quality of our prior knowledge $\rho(m_0)$. Conversely, if $d(m_0)$ is insensitive to m_0 (Figures 1c and 1d), the posterior PDF, $\sigma(m_0)$, will be entirely determined by our *a priori* information on m_0. In reality, we typically deal with intermediate situations in which our prior knowledge is somewhat vague, the physical theory imperfect, and the sensitivity of geophysical observables to some or all parameters of interest is often nonlinear and relatively weak. Although $L(\mathbf{m})$ usually can be determined in a straightforward manner, the choice of $\rho(\mathbf{m})$ is not trivial and often controversial [e.g., *Scales and Tenorio*, 2001; Kitanidis, 2011a,2011b]. In essence, $\rho(\mathbf{m})$ has to describe (i) everything we know about the problem that is independent of the observed data and (ii) how certain we are about this knowledge. This prejudice can affect (bias) our evaluation of $\sigma(\mathbf{m})$ to a large extent when the observables at hand are not strongly sensitive to changes in model parameters.

[23] This paper focusses on the information that controls the estimations of $L(\mathbf{m})$ and $\rho(\mathbf{m})$ during the inversion of geophysical data for the thermochemical structure of the lithosphere and sublithospheric upper mantle. The likelihood function $L(\mathbf{m})$ depends not only on the chosen data (i.e., geophysical observables), their associated uncertainties, and their intercorrelations but also on the physical theory relating these data to model parameters; the prior $\rho(\mathbf{m})$ is controlled by our current understanding of mantle composition, thermal state, and thermophysical properties. An accompanying paper [*Afonso et al.*, part II, this volume] discusses in detail the general inversion methodology in full 3-D geometry, its computational implementation (LitMod_4I), and synthetic examples. Readers interested in the entire methodology will benefit from reading parts I and II together. The application of the method to a real-case scenario will be presented in a forthcoming publication [*Afonso et al.*, part III].

2. The *A Priori* Information: Compositional Parameters

[24] Any information about the model parameters and data acquisition/processing that is independent of the actual results of measurements (i.e., data values) can be treated as *a priori* information. It is customary in geophysical studies to distinguish between *a priori* information on model parameters **m** and on observable parameters **d** or data. The former often consists of an idea or prejudice about possible distributions and associated uncertainties for the model parameters, while the latter is related to the uncertainties affecting the actual measurements. We refer the reader to *Duijndam* [1988] and *Tarantola* [2005] for more detailed discussions. We note here, however, that when a joint PDF $\rho(\mathbf{d}, \mathbf{m}) = \rho_M(\mathbf{m})\rho(\mathbf{d})$ can be defined, the prior PDF $\rho(\mathbf{d})$ becomes part of the likelihood function $L(\mathbf{m})$ (equation (7)) [*Mosegaard and Tarantola*, 2002]. Therefore, we will deal with this PDF when discussing $L(\mathbf{m})$ in context of the actual data and geophysical observables. In this section, we focus on the definition of the compositional parameters included in our vector **m**, their associated $\rho(\mathbf{m})$, and how to explore them (by generating random and statistically independent samples) in an efficient manner.

2.1. The Crust: Independent Information

[25] Being the shallowest solid layer of the Earth, the continental crust has been extensively studied by geochemical, geophysical, petrological, and structural means. Entire sections down to lower crustal levels are accessible to direct observation/sampling in many orogenic belts [cf.

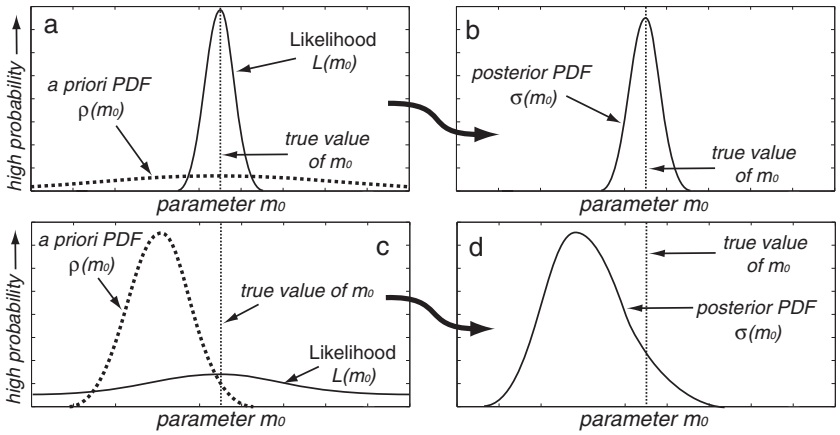

Figure 1. The posterior PDF is proportional to the product of $L(m_0)$ and $\rho(m_0)$. (a and b) Case where the observable is strongly sensitive to variations in the target parameter (m_0) and our prior information on model parameters is poor. The posterior PDF is controlled by $L(m_0)$ and it offers a good estimate of the true value. (c and d) Case where our prior knowledge of the parameter space is incorrectly biased towards wrong values and the observable is weakly sensitive to variations in the target parameter (m_0). The posterior PDF is controlled by our faulted prior information and therefore the posterior PDF provides a high probability to wrong values.

Salisbury and Fountain, 1990], and abundant xenoliths have been carried to the surface in many volcanoes and igneous provinces around the world [e.g., *Rudnick and Gao*, 2004]. Consequently, there is an extensive bibliography not only on the compositional structure of the continental crust [cf. *Taylor and McLennan*, 1985; *Rudnick*, 2004] but also on its average physical properties [cf. *Meissner*, 1986; *Rudnick*, 2004; *Brown and Rushmer*, 2006]. Since the main interest of the present study is the inaccessible thermal and compositional structure of the underlying subcontinental mantle, we will not deal with the detailed structure of the crust. Robust information on the latter can be obtained through independent studies, such as active-source seismic surveys, ambient noise tomography (ANT), gravity surveys, and/or field analysis. Nevertheless, since some of the geophysical observables used in our method are sensitive to crustal structure through their implicit or explicit integrating property (particularly Moho depth and average density and conductivity), its signature has to be either "removed" (i.e., filtered) or explicitly accounted for in the inversion scheme. Ideally, we will have access to high-quality information on the crustal structure when modeling a particular region, and therefore, its effects can be accounted for in the inversion process. When this is not the case, however, the crustal structure itself becomes an unknown that has to be obtained from the inversion scheme. Optimal parameterizations and *a priori* information used when inverting for crustal structure are discussed in detail in paper II [*Afonso et al.*, this issue].

2.2. The Lithospheric Mantle: Melt Depletion and Refertilization

[26] The four main mineral phases in the upper mantle are olivine, clinopyroxene, orthopyroxene, and an Al-rich phase. The latter can be either garnet, spinel, or plagioclase depending on the equilibration pressure and typically defines the "facies" from which the samples have been recovered (e.g., garnet facies). Secondary phases, such as apatite (phosphate), rutile (TiO_2), zircon ($ZrSiO_4$), monazite (phosphate), phlogopite (Mg-rich mica), and amphibole (hydrous silicate) are also common, although their combined mode rarely amounts to more than 5% of the total assemblage, except in localized veins or strongly metasomatized samples [cf. *Nixon*, 1987; *Pearson et al.*, 2004]. The four main mineral phases are complex solid solutions that accommodate different amounts of the major elements (e.g., Si, Al, Mg, Fe, and Ca) in their lattice depending on temperature, pressure, and bulk composition. The physical properties of a solid assemblage thus depend not only on the volumetric proportions (modes) of the constitutive mineral phases and environmental variables (e.g., oxygen fugacity and stress/strain state) but also on their individual compositions (e.g., fayalite content in olivine).

[27] Although the bulk composition of the lithospheric mantle can be represented as that of a peridotite *sensu lato*, processes such as melt extraction and/or melt percolation can change this average composition considerably [cf. *Griffin et al.*, 1999, 2009]. Moreover, solidified melts within the lithospheric mantle coupled with fluid-rock interaction processes can result in local, but significant, lithological contrasts (e.g., eclogite and/or pyroxenite bodies, Appendix A; SiO_2-enriched harzburgitic domains) [*Kelemen et al.*, 1998; *Jacob*, 2004; *Pearson et al.*, 2004; *Bodinier et al.*, 2008].

[28] The terms "depleted" and "fertile" are commonly used to describe the degree to which the composition of a peridotite has been modified, relative to some assumed starting composition, by melt extraction and/or metasomatism. Although these two processes affect both the trace-element and major-element abundances of the residual peridotite, most of the thermophysical properties of interest for geophysical methods are dependent only on the major-element composition. This is because the major-element abundances control the modal composition of the rock (i.e., mineral abundances), which in turn controls its thermophysical properties. Trace elements, on the other hand, can provide crucial information on the nature and timescale of melting and metasomatic events [e.g., *Hofmann*, 1997; *Stracke and Bourdon*, 2009], but their effects on the mineral assemblage are nil.

[29] Despite second-order discrepancies between different melting models/experiments, the general "depletion pattern" of the five main oxides SiO_2-Al_2O_3-MgO-FeO-CaO is well understood, and their atomic ratios are typically used to quantify the degree of depletion in peridotites [cf. *Herzberg*, 2004; *Pearson et al.*, 2004]. Amongst these, the ratio between MgO and FeO, the so-called "magnesium number" (Mg# = MgO/[MgO + FeO]) is of particular interest given that (i) together with SiO_2, FeO and MgO typically account for more than 95% by weight of peridotites and thus exert a major control on modal compositions, (ii) the ratio MgO/FeO shows a distinctive increase with melt extraction, and (iii) MgO and FeO have a strong influence on the relative abundances of mineral end members of volumetrically dominant phases (e.g., olivine and pyroxenes). During melt extraction, the Mg# of the residue increases almost linearly with degree of melting, regardless of whether melting is a batch or a fractional process and/or whether it occurs under wet or dry conditions [*Hirose and Kawamoto*, 1995; *Herzberg and O'Hara*, 2002; *Herzberg*, 2004]. Also, mainly due to (i) and (iii) above, there are clear correlations between the residue's Mg# and its bulk density, shear and compressional velocities, and electrical conductivity [e.g., *Lee*, 2003; *Speziale et al.*, 2005; *Matsukage et al.*, 2005; *Jones et al.*, 2009; *Afonso et al.*, 2010]. Unfortunately, FeO can be reintroduced into the solid assemblage during metasomatism by infiltration of mafic melts [*Griffin et al.*, 2009], which results in an overall reduction of the residue's Mg#. CaO and Al_2O_3 are also commonly added to the system by such processes. The metasomatic reintroduction of incompatible elements back into the residue is referred to as "refertilization." Therefore, the Mg# of peridotites should not be seen as a measure of melt depletion only but as an overall indicator of depletion + refertilization. However, the correlations between the residue's Mg# and its physical properties remain valid regardless of whether the Mg# is a consequence of depletion, refertilization, or a combination of these processes.

[30] An important compositional indicator that has received much less attention in the geophysical literature is Al_2O_3. This oxide exerts a strong influence on the bulk density (mainly through its control on garnet mode) and seismic velocities of peridotites, and it correlates well with other depletion indicators (section 2.3). As shown in paper II, the identification of "Al_2O_3-anomalies" may be more practical and informative than those associated

with FeO and/or MgO contents when inferring upper mantle compositional domains through inversion of multiple geophysical observables.

[31] Another incompatible "element" that affects the physical properties of the mantle is water. Water is two to three orders of magnitude more soluble in melts than in mantle minerals [cf. *Hirschmann*, 2006]. Consequently, considering typical water contents in mantle rocks (<200–400 ppm), melt extractions of only <10% can effectively "dry out" the residue, significantly increasing its electrical resistivity and viscosity relative to its hydrated counterpart [e.g., *Karato*, 2008; *Jones et al.*, 2012]. Note, however, that the expected average water contents of <400 ppm in subcontinental mantle rocks do not affect other relevant physical parameters (Vs, Vp, density) to any significant extent (Appendix B).

[32] Another side effect of melt extraction is the removal of the highly incompatible radioactive elements K, Th, and U from the lithospheric mantle. The total contents of these heat-producing elements determine the relative mantle contribution to the SHF and the temperature distribution with depth in the lithosphere. Although it is usually expected that highly depleted Archean xenoliths would have the lowest concentrations of these elements, some compilations of cratonic, off-craton, and massif peridotite xenoliths [*Rudnick et al.*, 1998] found an inverse correlation. These authors interpreted this "anomalous" behavior as being a consequence of several issues, such as postextrusion chemical alteration, analytical detection limits, and sampling bias. However, *Rudnick et al.* [1998] concluded that the average content of K, Th, and U from analyzed cratonic samples cannot be representative of the heat production of Archean mantle roots. This indicates that melt extraction processes are masked, in the case of these radioactive elements, by refertilization processes, and therefore, the amount of melt extraction cannot be estimated or accounted for by means of mass balance methods. Interestingly, anomalously high contents of K, Th, and U in the lithospheric mantle, as suggested by some xenoliths, could locally increase the temperature of the lithosphere above typical conductive geotherms and produce detectable signatures in geophysical observables [*Hieronymus and Goes*, 2010].

2.3. Correlations Among Major Oxides

[33] From the previous section, we can expect the major-element contents of peridotites to be correlated to some degree along melting or refertilization paths. In this section, we show that this holds true in real samples, which allows us to derive statistical correlations between the five main major oxides in such a way that only two key element contents will be needed as free compositional parameters in our inversion scheme in order to derive the entire set of thermophysical properties for a peridotitic rock.

[34] Figure 2 shows covariation plots of the main five oxides in peridotites from a large database ($n > 2900$) that includes xenoliths from both subcontinental lithospheric mantle (SCLM) and oceanic mantle as well as samples from orogenic massifs and ophiolites (references in the Supporting Information). The Mg# of these samples ranges from ~ 84 to 96, thus covering most of the expected variability in mantle peridotites, from fertile (or refertilized) lithospheric mantle to highly depleted harzburgites and dunites from the Archean SCLM. Importantly, the negative correlation observed in the Al_2O_3-MgO and CaO-MgO plots is one of the most robust features observed in peridotites and is commonly interpreted as the result of either melt

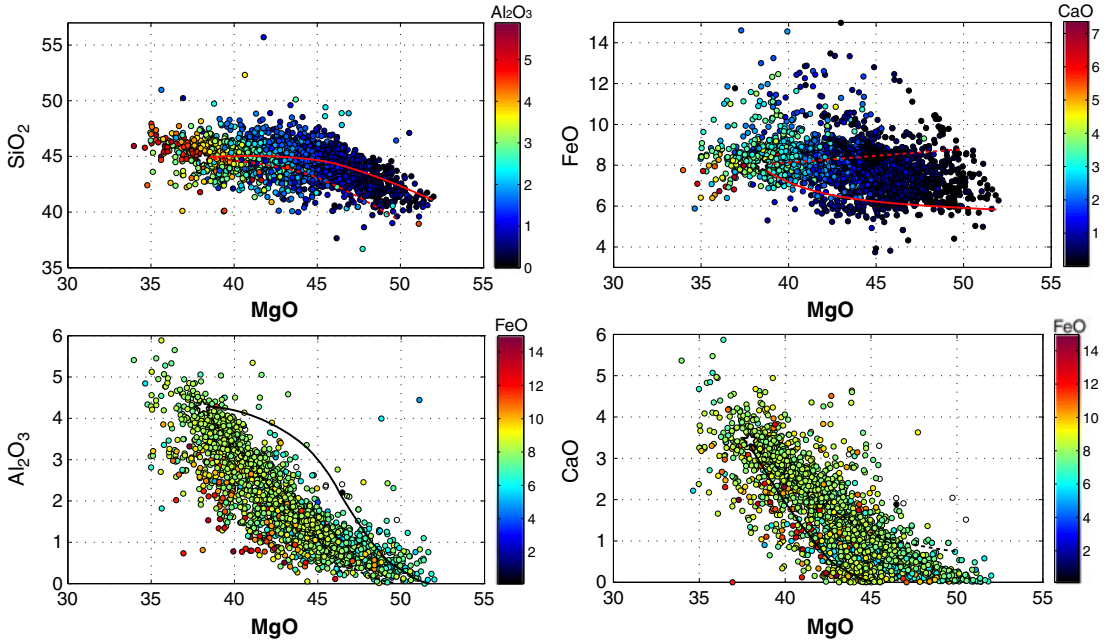

Figure 2. Covariation plots for our dataset ($n > 2900$). The color scales represent the content of a third oxide. Two polybaric perfect fractional melting paths [*Herzberg*, 2004] with different initial pressures of melting are included for comparison; dashed line = 2 GPa, solid line = 7 GPa. The initial fertile composition for these melting paths is indicated by the white star.

depletion, late re-enrichment events, or a combination of both [cf. *Griffin et al.*, 2009].

[35] Figure 3a shows a covariation plot of MgO and Al_2O_3 for our entire dataset. We have regressed the data with both linear and polynomial models using a robust regression method based on an iterative weighted least-squares algorithm with a bisquare weight function [*Rousseeuw and Leroy*, 2003]. The final fitting model obtained with this method is less sensitive to outliers in the data as compared with ordinary least-squares methods. The best model was obtained with a second-order polynomial regression, which gives the lowest root mean square errors and the highest R^2 value ($R^2 = 0.772$), respectively. A linear regression gives a $R^2 = 0.751$, while higher-order polynomials overfit the data. Figure 3c also includes the 95% confidence interval of the predicted values. The meaning of this interval is straightforward. If one has a new sample for which the Al_2O_3 content is 3 wt%, then its MgO content has a 95% probability of being between 37.5 and 42.5 wt% (i.e., between the two confidence intervals). In addition, it is clear from the data that the probability (or frequency) between these two limits is not homogeneous, but it tends to follow a quasi-normal distribution. This is shown in Figures 3d and 3e, which contain the frequency distribution for two Al_2O_3 bins, each 1% wide. For comparison, Figures 3d and 3e include two curves indicating the theoretical distributions of two particular cases of the generalized Gaussian distribution: Laplacian (i.e., double exponential) and Gaussian (i.e., normal).

[36] A similar analysis can be applied to the covariation of CaO and Al_2O_3 (Figure 4). In this case, there is no noticeable improvement when fitting the data with higher-order models than linear. The result of a robust linear regression is shown in Figure 4c, together with the two 95% confidence limits. As in the previous case, the distribution between these confidence limits is not homogeneous but follows a quasi-normal distribution (Figures 4d and 4e).

[37] In contrast to CaO and MgO, SiO_2 and FeO do not exhibit any significant correlation with either Al_2O_3 or CaO. Although the data show a tendency for SiO_2 and FeO

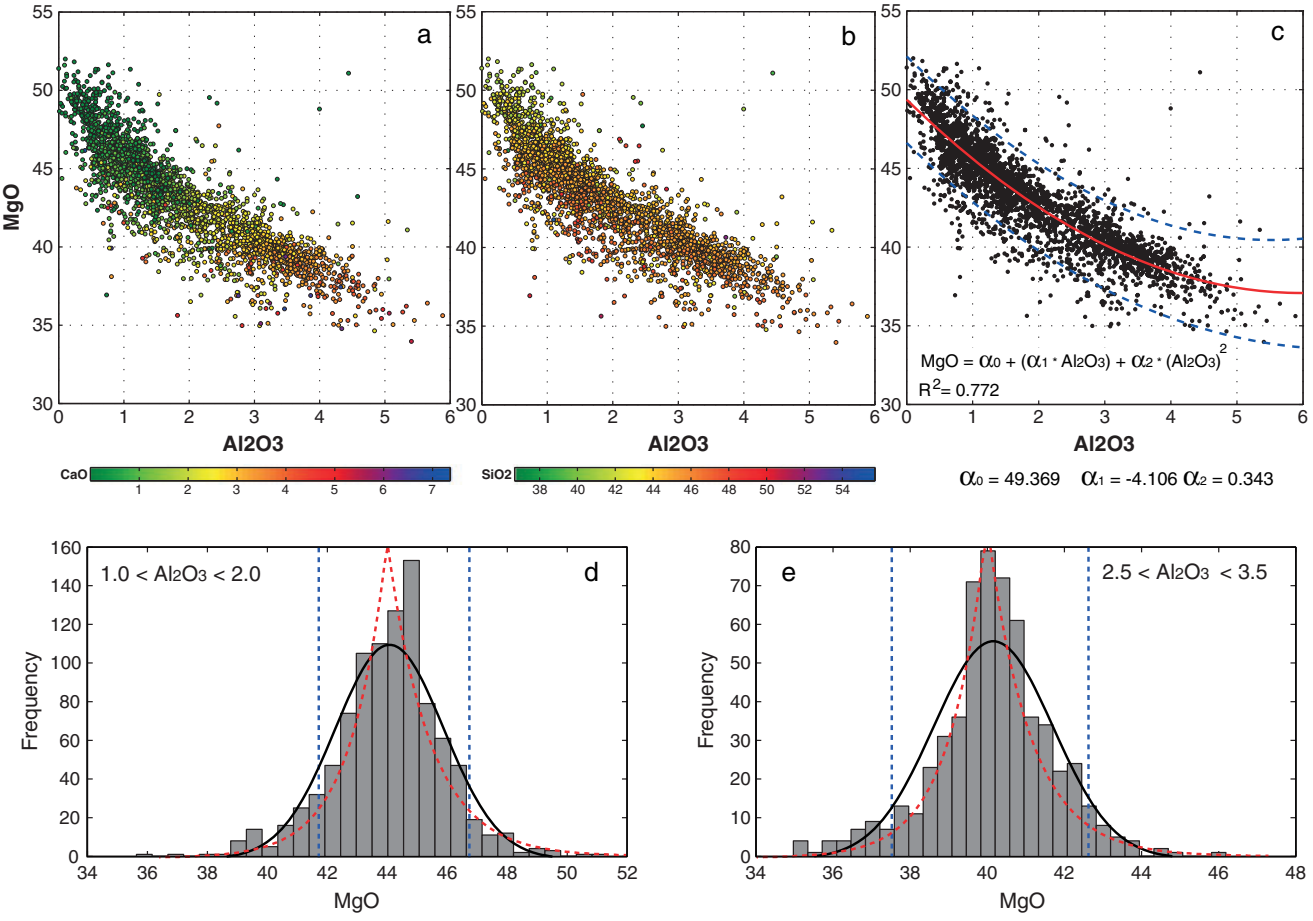

Figure 3. Covariation plot of MgO with Al_2O_3 for all samples in our dataset. (a) Color scale indicates the content of CaO. (b) Color scale indicates the content of SiO_2. (c) Results from a second-order polynomial robust regression. Solid red line denotes the second-order polynomial fit; blue dashed lines denote the 95% confidence limits from the regression. (d and e) Histograms of MgO content for two different Al_2O_3 bins (from Figure 3a). The black solid lines are best-fitting Gauss (i.e., normal) distributions; the red dashed lines are best-fitting Laplace (i.e., double exponential) distributions. The 95% confidence limits are shown as blue dashed lines.

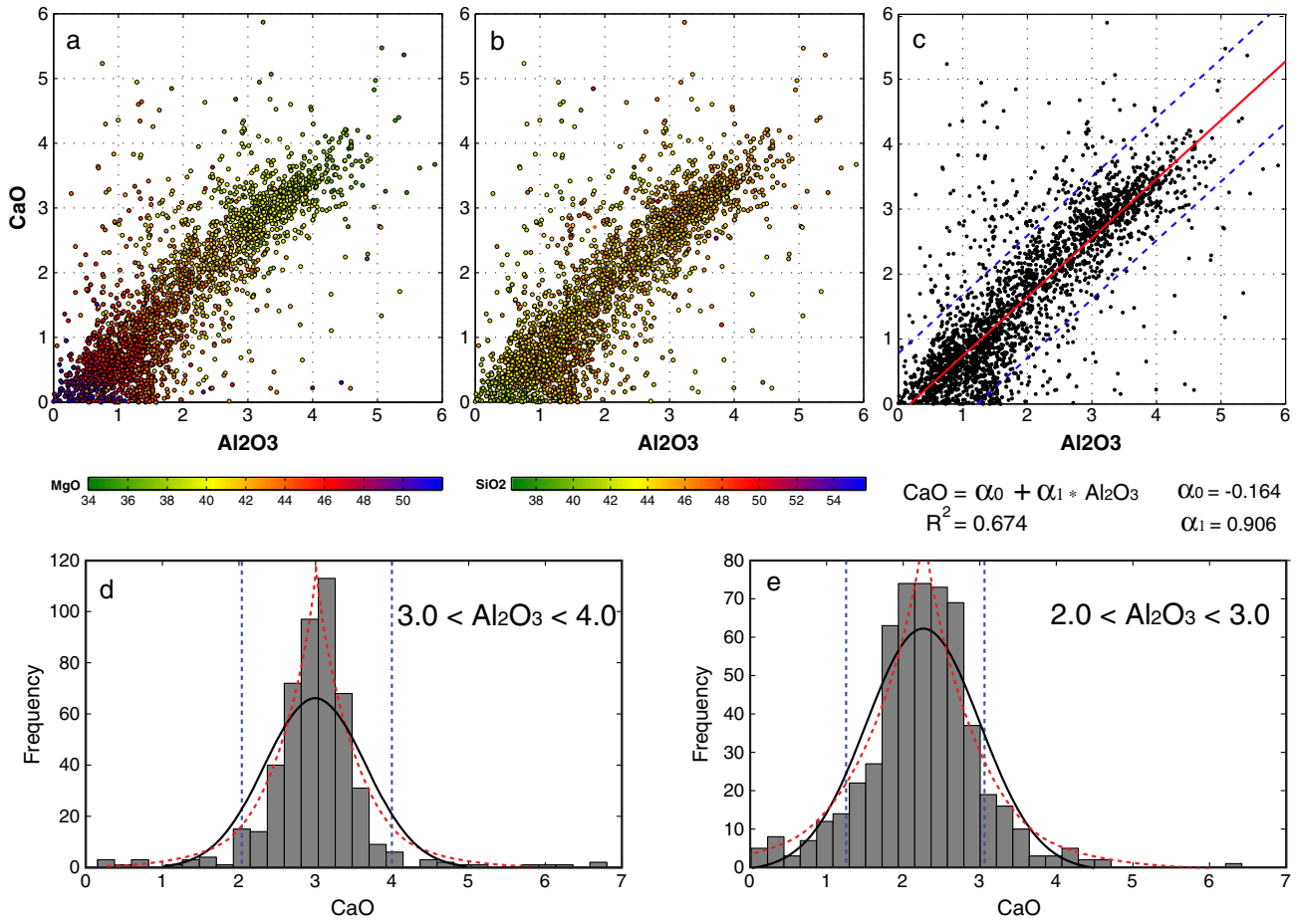

Figure 4. Covariation plot of CaO with Al_2O_3 for all samples in our dataset. (a) Color scale indicates the content of MgO. (b) Color scale indicates the content of SiO_2. (c) Results from a linear robust regression. Solid red line denotes the linear fit; blue dashed lines denote the 95% confidence limits from the regression. (d and e) Histograms of CaO content for two different Al_2O_3 bins (from Figure 4a). The black solid lines are best-fitting Gauss (i.e., normal) distributions; the red dashed lines are best-fitting Laplace (i.e., double exponential) distributions. The 95% confidence limits are shown as blue dashed lines.

to increase with Al_2O_3 and decrease with MgO, in accordance with melting systematics, robust regression yields R^2 values $\lesssim 0.1$ for both cases. This lack of correlation in natural samples reflects the interplay between mineral chemistry, modes, and bulk composition. High-Mg olivine or orthopyroxene will have higher SiO_2 contents (on a wt% basis) than the Fe-rich end member of each solid-solution series. On the other hand, in mantle peridotites, higher FeO contents typically are found in more fertile rocks, which will have higher ratios of pyroxene (both opx and cpx) to olivine, raising SiO_2 contents and countering the effect of Fe/Mg variations.

[38] Monte Carlo methods for sampling or exploring the parameter space of a model require the generation of many random and statistically independent realizations (samples). For our purposes, such realizations will involve generating random compositional samples (i.e., synthetic rock compositions) within the system CaO-FeO-MgO-Al_2O_3-SiO_2 (CFMAS). In the most general case, we could define wide lower and upper limits for the ranges of variation of each oxide, assign a uniform probability density to all values within this range, and then generate random samples for each of them with the constraint that the sum of all five oxides must add to 100%. This approach would unavoidably sample the entire parameter space, provided enough iterations are performed, including those regions that are "empty" in the data space (e.g., the region between 45 < MgO < 50 and 3 < Al_2O_3 < 4 in Figure 2). Conversely, when each oxide has a definite and known probability distribution, we could sample the compositional space much more efficiently by generating samples according to these distributions, thus avoiding oversampling regions of low probability.

[39] In principle, the histograms in Figure 5 suggest possible distributions. However, it is entirely possible, indeed likely, that these distributions are the result of a sampling bias in existing databases, including ours. In particular, the double peaks in Al_2O_3 and CaO are controlled by the Archean and Phanerozoic xenolith populations, which tend to be numerically dominant in most global databases. This is simply because kimberlites, which preferentially

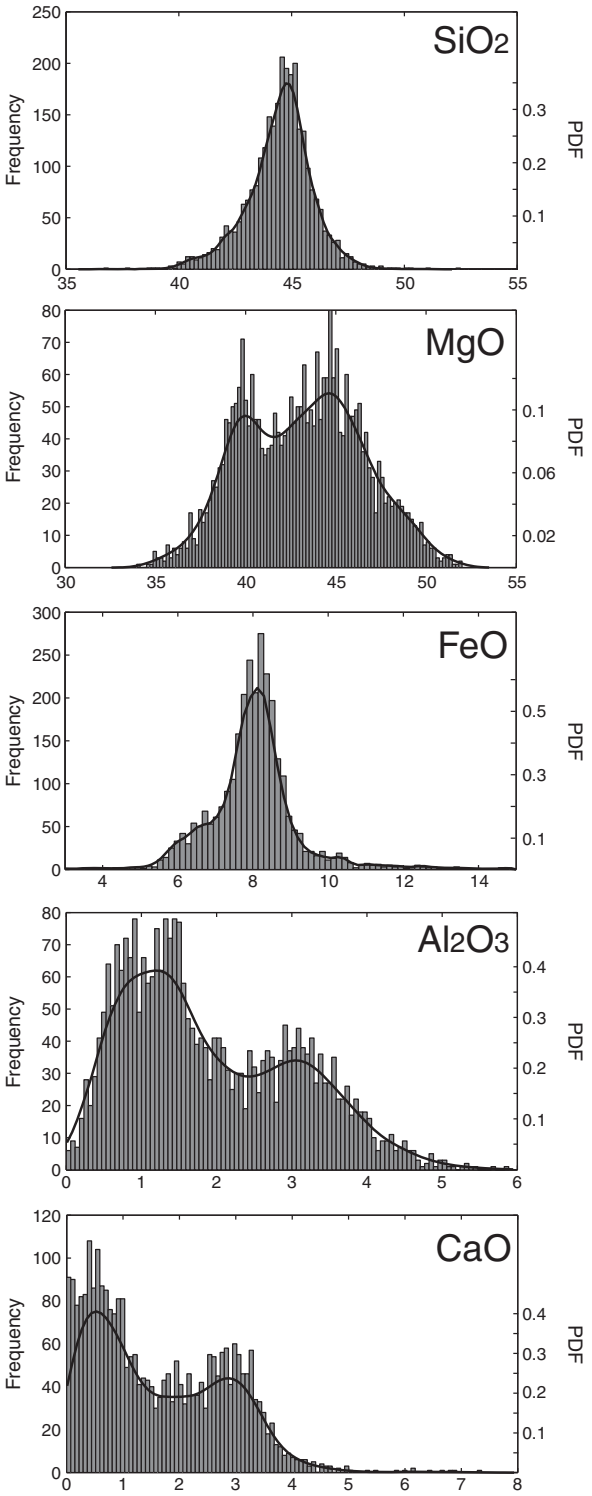

Figure 5. Histograms for the five major oxides in our entire dataset (shown in Figure 2). Best-fitting density distributions are shown for each case. The latter have been calculated with a Gaussian kernel density estimator [*Venables and Ripley*, 1999]. If these probability densities were used to generate samples of the compositional space, samples with Al_2O_3 contents ∼1 would have much higher probabilities than samples with Al_2O_3 contents >2. However, this is a fictitious effect due to the dominance of "Archean" samples in the database (see text).

sample stable cratonic areas, and alkali basalts, which tend to sample young intraplate settings, are the most prolific sources of mantle xenoliths. By contrast, xenolith-rich volcanic rocks are relatively rare in collisional settings (e.g., island arcs), so these environments are under-represented in xenolith databases.

[40] There are other built-in biases in xenolith datasets. Alkali basalts typically sample shallow, less depleted mantle, with few samples from deeper than approximately 60 km; garnet-bearing ultramafic xenoliths are rare or absent in most localities. Kimberlites typically sample down to depths of $\gtrsim$180 km, but most studies of kimberlite-borne xenoliths have focussed on garnet-bearing samples, partly because they are amenable to P-T estimation; these xenoliths are all from depths greater than approximately 80–100 km. Shallower and/or more depleted (hence garnet-free) cratonic mantle is strongly under-represented in the published record. Published databases on kimberlite-borne ultramafic xenoliths also have been strongly dominated until recent years by the abundant material from a small number of kimberlites in the Western Terrane of the Kaapvaal Craton (Kimberley area), where mining has produced a veritable mountain of xenolith debris. Many of these samples are highly enriched in orthopyroxene (high opx/oliv), and it has been argued that the low FeO content of "average Archean" peridotites (Figure 2) simply reflects dilution by orthopyroxene, rather than high-P melting [*Simon et al.*, 2007; *Pearson and Wittig*, 2008]. However, the distinctive low FeO contents of peridotite xenoliths from Archean cratons are also observed in suites from North America, Siberia, and even other terranes of the Kaapvaal craton (e.g., N. Lesotho) where enrichment in orthopyroxene is not common [*Griffin et al.*, 1999, 2009].

[41] Bearing in mind these considerations, any method that relies on *a priori* PDFs based on specific compilations or on compositional/tectonic *regionalizations* (e.g., Archean domains are assigned "Archean-like" compositions) cannot be considered entirely general. We therefore adopt a sampling approach intermediate between the two extreme sampling examples described above. Since statistically significant correlations between Al_2O_3 and CaO and Al_2O_3 and MgO are found in all published compilations of peridotitic samples, regardless of their tectonic environment and/or facies (see references in the Supporting Information), we assign more weight to these correlations (Figures 3 and 4) than to any specific univariate or multivariate probability distribution (e.g., Figure 5). Therefore, in order to generate random, statistically independent, and representative compositional samples during our inversions, we proceed as follows:

[42] (i) Choose a wide initial variation range for Al_2O_3 and FeO that covers >95% of the entire natural variability, and assign a uniform probability density within these ranges (i.e., equal probability to all values within the chosen range). Typically, we will use $0 < Al_2O_3 < 5.5$ and $5 < FeO < 11$ (Figure 2), but these can be easily updated as more data is included in the database.

[43] (ii) Select a value for Al_2O_3 and FeO within their respective variation ranges using a random sampler.

[44] (iii) Use the selected Al_2O_3 value with the Al_2O_3-MgO and Al_2O_3-CaO regressions derived above (Figures 3

and 4) to obtain a preliminary (mean) value for MgO and CaO.

[45] (iv) Randomly select a new value for MgO and CaO from the known probability distributions associated with each Al_2O_3 value (Figures 3d and 3e and 4d and 4e). Typically, we will use a Gaussian distribution.

[46] (v) Calculate the SiO_2 content of the present sample as 100 – (FeO + CaO + MgO + Al_2O_3).

[47] This approach generates independent random samples that cover the entire compositional spectrum observed in real mantle samples, without oversampling low-probability regions. Since it is based on well-established correlations between oxides (Figures 2–4) instead of whole-data PDFs (Figure 5), it is less sensitive to biases in the dataset. Importantly, only two free parameters (Al_2O_3 and FeO), instead of four, are needed in the random search to obtain a complete representative compositional sample. As we show in paper II [*Afonso et al.*, this volume], this feature is particularly useful when performing the full non-linear inversion in 3-D geometry, without compromising the results to any extent in comparison to a full search with four-free parameters.

3. Mineral Assemblages and Inexact Physical Theories

[48] As stated in section 1, the evaluation of the likelihood function $L(\mathbf{m})$ depends not only on the chosen observables and their uncertainties but also on the physical theory used to relate these observables to the model parameters. The problem of predicting the values of observable parameters $\mathbf{d} = (d_1, d_2, \ldots d_n)$ that would correspond to a certain model $\mathbf{m} = (m_1, m_2, \ldots m_n)$ is known as the *forward problem*. In other words, the forward problem maps $\mathbf{m}$ into $\mathbf{d}$ through an operator $\mathbf{g}(\cdot)$. This mapping, which can be non-linear, is usually written as $\mathbf{d} = \mathbf{g}(\mathbf{m})$ [*Tarantola*, 2005]. The operator $\mathbf{g}$ typically represents more than one physical theory (e.g., heat transfer and potential field), and the connection between them can be complex. In general, $\mathbf{g}$ will not represent an exact (i.e., error-free) or perfect theory, and therefore, it will be subject to modelization errors. However, the question of how to describe or quantify these errors is not straightforward and depends on the actual theory and model discretization (see below).

[49] In this work, the operator $\mathbf{g}$ is composed of suboperators associated with the solution of the following forward problems: Gibbs energy minimization $\mathbf{g}_G$, heat transfer $\mathbf{g}_T$, Maxwell's equations $\mathbf{g}_M$, gravity potential $\mathbf{g}_P$, Love and Rayleigh dispersion curves $\mathbf{g}_D$, and isostasy $\mathbf{g}_I$. An important part of the theoretical uncertainties associated with $\mathbf{g}_G$, $\mathbf{g}_T$, $\mathbf{g}_I$, and $\mathbf{g}_M$ are intimately related to the actual physical theory (e.g., adopted solid-solution models, electrical conductivity as function of bulk composition, and local isostasy assumption) or assumed thermal parameters (e.g., radiogenic heat production and thermal conductivity), rather than to the discretization of the model. Here, we discuss briefly the theoretical uncertainties of $\mathbf{g}_G$, $\mathbf{g}_M$, $\mathbf{g}_I$, and $\mathbf{g}_T$ that arise during the computation of the governing physical parameters (e.g., electrical conductivity); those dominated by the discretization of the model and/or the numerical technique used to solve the governing equations will be discussed in detail in paper II.

3.1. Gibbs Energy Minimization ($\mathbf{g}_G$)

[50] The thermodynamic (Gibbs energy minimization) operator $\mathbf{g}_G$ is used to obtain mineral assemblages from major-element compositions and given P-T conditions. The equilibrium mineral assemblages of all relevant ultramafic lithologies (i.e., eclogite, pyroxenites, and peridotites) and their relevant physical properties are computed with components of the software Perple_X [*Connolly*, 2009] within the CFMAS system using the database and thermodynamic formalism of *Stixrude and Lithgow-Bertelloni* [2011]. The CFMAS system accounts for $\gtrsim$98 wt% of the Earth's crust and mantle, and therefore, it is considered to be an excellent starting basis for modeling phase assemblages in the Earth. More complete systems, including, e.g., Na_2O and H_2O, can also be easily included in our method. However, as we show in Appendix B, the added value of including additional elements in our computations is insignificant when compared with the increase in computational time.

[51] The estimation of the uncertainties associated with the computation of the mineral assemblages (i.e., mineral modes and their compositions) and their physical properties can, in principle, be done by comparing laboratory observations with predictions. In practice, however, this is problematic for two main reasons: (i) available laboratory "observations" on modal proportions of ultramafic rocks are subject to measurement uncertainties that are of the same order (sometimes significantly larger) as those related to the modeling [cf. *El-Hinnawi*, 1966] and (ii) the lack of a large population of well-studied representative mantle samples for which modal proportions, mineral chemistry, and physical properties have been measured with high precision at high P-T conditions. Typically, mineral modes of real samples are estimated either by point-counting techniques [cf. *El-Hinnawi*, 1966] or from bulk and mineral chemical analyses by solving a least-square problem with assumed density values for each phase. Although the uncertainties associated with these techniques depend on the actual analyses and individual phase analyzed, values between 1 and 3 wt% for two standard deviations are common. To illustrate the statement in point (i) above, we compare predicted and "observed" modal compositions (Table 1) for 10 representative xenoliths that span most of the compositional range in our database (see also *Afonso and Schutt*, 2012). In most cases, the difference between our predictions and the "observed" values is within the experimental error, and when this is not the case, the difference is negligible in terms of the associated changes in physical properties.

[52] In this study, we use the standard Voigt-Reuss-Hill average for computing the elastic properties of the solid assemblage. A number of studies in which modes and elastic properties of polyphase materials have been measured and compared with predictions from physical theories of composites suggest that, as long as the modes are properly accounted for and the elastic parameters of the constituent phases are well known, predictions are typically within $\pm$1.2% [e.g., *Ji et al.*, 2003a; *Ji*, 2004; *Afonso et al.*, 2005; *Naus-Thijssen et al.*, 2011]. Interestingly, this value is comparable to the differences between predictions from standard theories of composites and from different mineral physics methods used to calculate the seismic properties of

Table 1. Comparison Between "Observed" and Calculated Modes for 10 Representative Samples From our Database[a]

Sample	phase	obs.	calc.	Δ%	2STD
KGG13	Ol	68	68	0	2.48
	Opx	13	15	*2*	1.79
	Cpx	12	11	1	1.73
	Gt	7	6	1	1.36
KGG14	Ol	63	61	2	2.57
	Opx	11	14	*3*	1.66
	Cpx	10	9	1	1.60
	Gt	16	16	0	1.95
KGG06	Ol	72	71	1	2.39
	Opx	11	13	*2*	1.66
	Cpx	9	8	1	1.52
	Gt	8	8	0	1.44
KGG83	Ol	79	75	*4*	2.17
	Opx	9	14	*5*	1.52
	Cpx	5	5	0	1.16
	Gt	7	6	1	1.36
KGG88	Ol	72	68	*4*	2.39
	Opx	20	24	*4*	2.13
	Cpx	4	4	0	1.04
	Gt	4	4	0	1.04
FRB1684	Ol	69	72	*3*	2.46
	Opx	22	20	2	2.20
	Cpx	5	4	1	1.15
	Gt	4	4	0	1.04
FRB1685	Ol	63	65	2	2.57
	Opx	28	27	1	2.39
	Cpx	4	3	1	1.04
	Gt	5	5	0	1.16
PHN5304	Ol	73	76	*3*	2.36
	Opx	19	16	*3*	2.09
	Cpx	3	4	1	0.91
	Gt	5	4	1	1.16
PHN5316	Ol	60	60	0	2.61
	Opx	23	24	1	2.24
	Cpx	7	7	0	1.36
	Gt	10	9	1	1.60
U506	Ol	77	75	2	2.24
	Opx	16	18	2	2.01
	Cpx	3	3	0	0.91
	Gt	4	4	0	1.04

[a]The thermodynamic database and formalism are that of *Stixrude and Lithgow-Bertelloni* [2011]. All samples are garnet-bearing peridotites (KGG13, KGG14, KGG06, KGG83, and KGG88 from *Franz et al.* [1996]; FRB1684, FRB1685, PHN5304, and PHN5316 from *Boyd et al.* [2004]; and U506 from *Ionov et al.* [2010], see references in the Supporting Information). Δ% is the absolute difference in modal percent between calculated and "observed" modes; 2STD is an estimation of the absolute error associated with the "observed" values (2 standard deviations) computed as $1.85 \times 0.6745\sqrt{k(100-k)/n}$, where k is the estimated mode of the phase in % and n the number of point counts, here assumed = 550 [*El-Hinnawi*, 1966]. Δ% values larger than 2STD are shown in italics.

rocks [*Ji*, 2004; *Schutt and Lesher*, 2006; *Afonso et al.*, 2008; *Afonso and Schutt*, 2012].

3.2. Electrical Conductivity of Polymineralic Samples (g_M)

[53] Another important source of theoretical uncertainty arises from the calculation of the electrical conductivity of the assemblage ϵ. Several authors have recently reviewed the connection between the composition and temperature of peridotites, their water content, and their bulk electrical conductivity [e.g., *Xu et al.*, 2000; *Khan et al.*, 2006; *Jones et al.*, 2009, 2012; *Yoshino*, 2010; *Fullea et al.*, 2011, and references therein]. It is generally assumed that the dependence of σ on pressure, temperature, water content, and composition for each phase can be adequately modeled by an equation of the form

$$\epsilon = \epsilon_{\mathbf{0}} \exp\left(\frac{-\Delta H(X_{\mathrm{Fe}}, P)}{k_B T}\right) + \epsilon_{\mathbf{0i}} \exp\left(\frac{-\Delta H_i}{k_B T}\right) + f(C_w) \exp\left(\frac{-\Delta H_{\mathrm{wet}}(C_w)}{k_B T}\right) \quad (8)$$

where k_B is the Boltzmann constant and T the absolute temperature. The first to the third terms in the right-hand side of equation (8) describe the contribution from small polarons (i.e., electron hopping and its associated lattice distortion), the contribution of Mg vacancies at high temperatures, and the contribution by proton conduction (dependent on water content, C_w), respectively [cf. *Jones et al.*, 2012 and references therein]. Pre-exponential parameters ($\epsilon_{\mathbf{0}}$, $\epsilon_{\mathbf{0i}}$, $f(C_w)$) and activation enthalpies ($\Delta H(X_{\mathrm{Fe}}, P)$, ΔH_i, $\Delta H_{\mathrm{wet}}(C_w)$) are experimentally derived [cf. *Jones et al.*, 2009; *Fullea et al.*, 2011].

[54] *Fullea et al.* [2011] have recently evaluated the current experimental discrepancies between different laboratories and their impact on the calculation of σ for each phase. Using the maximum discrepancies between different experimental models of ϵ as a proxy, we can assign the following compositional uncertainties to each phase: $\Delta\epsilon_{\mathrm{ol}} = 0.35$ for olivine; $\Delta\epsilon_{\mathrm{opx}} = \Delta\epsilon_{\mathrm{cpx}} = 0.46$ for clinopyroxene and orthopyroxene; and $\Delta\epsilon_{\mathrm{gt}} = 0.44$ for garnet. Here, each $\Delta\epsilon$ represents a first-order estimate of the standard deviation associated with log units (i.e., $\log(\epsilon)$). The propagation of these phase uncertainties to the final estimation of the bulk rock electrical conductivity $\epsilon_{\mathbf{T}}$ depends on the actual averaging method employed to calculate $\epsilon_{\mathbf{T}}$. *Berryman* [1995] and *Jones et al.* [2009] have discussed the available methods for estimating the electrical conductivity of multiphase materials and concluded that the Hashin-Shtrikman extremal bounds are the most reliable approach. In practice, the two extreme bounds are rather similar and therefore their geometric mean can be taken as the best estimate of $\epsilon_{\mathbf{T}}$ for most purposes. Using these equations and typical modal compositions for peridotites, a standard error propagation analysis results in a representative estimate of $\Delta\epsilon_{\mathbf{T}} \sim 0.4$. Note that this value includes the uncertainty associated with temperature ($\sim$0.3) [*Xu et al.*, 1998].

[55] For the purposes of the present work, water content C_w will be considered known *a priori* and constant. Future work will include C_w as an unknown to be retrieved from the inversion (Appendix B).

3.3. Isostasy and Elevation (g_I)

[56] The principle of isostasy is one of the oldest, best-tested, and most powerful concepts in geophysics [cf. *Turcotte and Schubert*, 1982; *Watts*, 2001]. Following *Afonso et al.* [2008] and *Fullea et al.* [2009], we compute absolute elevation under the assumption of local isostasy (see paper II for details). Except in regions of strong mantle

upwellings or subduction zones, local isostasy provides tight constraints on the average (integrated) mass of lithospheric columns with areas $\gtrsim 1 \times 10^4$ km^2 [*Lachenbruch and Morgan*, 1990; *Turcotte and Schubert*, 1982]. This holds true even when the wavelength of the density anomaly is less than 250–300 km, since corrections for flexural support can readily be made when gravity anomalies are available [e.g., *Fullea et al.*, 2009].

[57] It is common in the literature to distinguish between crustal, thermal, and dynamic compensation mechanisms [cf. *Phillips and Lambeck*, 1980; *Turcotte and Schubert*, 1982; *Nakiboglu and Lambeck*, 1985; *Lachenbruch and Morgan*, 1990; *Zhong*, 1997; *Hasterok and Chapman*, 2007], depending on the nature of the density anomaly compensating the associated topography. Of these three isostatic mechanisms, the first two typically account for more than 85% of the global surface elevation, regardless of whether local or regional isostasy assumptions are used in the computations [*Phillips and Lambeck*, 1980; *Mooney and Vidale*, 2003; *Kaban et al.*, 1999; *Fullea et al.*, 2009]. In crustal isostasy, the density contrasts controlling elevation are those between mantle and crustal rocks at the Moho and between air (or water) and surface topography. Thermal isostasy, on the other hand, refers to changes in topography due to temperature anomalies (strictly, to the associated thermal expansion) in all or parts of the lithosphere (not only in oceans!). When the lithosphere is defined as a thermal boundary layer, the terms thermal isostasy and lithospheric isostasy can be used interchangeably. Sublithospheric processes, such as plume impingement or forced convection, or intralithospheric processes, such as mantle delamination, can also modify surface topography through the generation and transfer of viscous stresses to the surface (the so-called "dynamic effects") [e.g., *Marquart and Schmeling*, 1989; *Lithgow-Bertelloni and Silver*, 1998; *Petersen et al.*, 2010]. Results from convection simulations indicate peak dynamic contributions to the total topography of the order of ∼400–800 m [*Marquart and Schmeling*, 1989; *Crameri et al.*, 2012] for relatively large plumes. However, these estimates need to be taken with caution, since convection computations rely on relatively uncertain parameters (e.g., asthenosphere viscosity and lithospheric strength) and in some cases, inaccurate numerical schemes [cf. *Crameri et al.*, 2012].

[58] Considering all of the above, we assign an average theoretical uncertainty of 15% to our computed elevation (with a minimum uncertainty of ±200 m), except in regions where evidence for large dynamic loads exists. In this case, higher local uncertainties or appropriate topographic corrections should be used.

3.4. Thermal Conductivity and Radiogenic Heat Production ($\mathbf{g}_T$)

[59] The main physical parameters controlling results from forward thermal modeling of the lithosphere are the radiogenic heat production *RHP* and thermal conductivity k_t of the rocks. Both these parameters are known to vary within relatively large ranges when different lithologies are considered. In particular, k_t of the main silicate minerals can vary from ∼1.6 to >7 W m^{-1} K^{-1} at room P-T conditions, although ∼90% of typical rocks exhibit k_t values of 2–4 W m^{-1} K^{-1} [cf. *Diment and Pratt*, 1988; *Clauser and Huenges*, 1995; *Jokinen and Kukkonen*, 1999; *Jaupart and Mareschal*, 2011]. Likewise, although *RHP* of typical lithospheric rocks can vary by as much as ∼0 to >10 μW m^{-3} between individual samples, regional averages (more suitable for lithospheric studies) are typically limited to *RHP* values <3.6 μW m^{-3} [*Vilá et al.*, 2010; *Jaupart and Mareschal*, 2011]. Using Monte Carlo simulations, *Jokinen and Kukkonen* [1999] showed that if the thermal conductivity and *RHP* of crustal layers can be estimated with standard deviations of 0.5–1.0 W m^{-1} K^{-1} and ∼2 μW m^{-3}, respectively, then the uncertainty in calculated temperatures within the lithosphere would amount to ±45–80°C. The uncertainties associated with calculated values of SHF, as estimated by these authors, are of the order of ±6–15 mW m^{-2}. Comparable, although somewhat larger, values were recently estimated by *Vilá et al.* [2010]. It therefore seems reasonable to assign minimum uncertainties of ±80°C and ±10 mW m^{-2} to temperature and SHF predictions from $\mathbf{g}_T$, respectively. We will typically use the same uncertainty values for temperatures at sublithospheric depths.

3.5. Putting Everything Into $\theta(\mathbf{d} \mid \mathbf{m})$

[60] With the above considerations, and in lieu of more detailed information, we ignore the uncertainty in the computation of mineral modes and phase composition associated with $\mathbf{g}_G$, since it is the smallest estimated uncertainty. For predictions of the aggregate's seismic properties, ϵ, temperature, elevation, and SHF, we will assume Gaussian PDFs of the form (refer to equation (7))

$$\theta(\mathbf{d} \mid \mathbf{m}) = \propto \exp\left\{-\frac{1}{2}(\mathbf{d}-\mathbf{g}(\mathbf{m}))^T C_t^{-1}(\mathbf{d}-\mathbf{g}(\mathbf{m}))\right\} \qquad (9)$$

where C_t is the covariance matrix describing the theoretical uncertainties. It is also expected that a certain amount of correlation exists between these theoretical uncertainties. We address these correlations and the computation of the full-rank C_t in paper II.

[61] An important problem that arises when calculating seismic velocities is the estimation of anelastic effects at high temperatures. Anelasticity in mantle rocks, and the associated attenuation of seismic waves, become important at temperatures >900°C [e.g., *Jackson et al.*, 2002; *Jackson and Faul*, 2010] . Since all of the sublithospheric upper mantle and up to ∼40% of the SCLM have temperatures higher than this limit, a correction to the anharmonic velocities obtained from the minimization problem is necessary. Unfortunately, experimental studies at relevant seismic frequencies and P-T conditions addressing the effects of grain sizes, volatile content, and bulk composition are either scarce or nonexistent. Moreover, meaningful comparisons between mineral physics models and observations are problematic due to the uncertainties affecting observations of seismic attenuation [e.g., *Dalton and Faul*, 2010] and, more importantly, the uncertainties in the average grain size and temperature structure of mantle sections. All these make it difficult, if not impossible, to objectively quantify the theoretical error associated with anelastic corrections. A first-order estimation of this error and its implementation in C_t are discussed in paper II.

4. Geophysical Observables: Sensitivity and Observational Uncertainties

4.1. Two Levels of Functional Relationships

[62] The fundamental goal of this study is the conversion of observations into robust estimates of temperature and composition in the lithosphere and sublithospheric upper mantle. This requires the assessment of two different but related levels of functional relationships (or parameterizations). The first is between the raw observations and the set of governing physical parameters, e.g., the physical relationship between travel times and the subsurface seismic velocity structure or between variations in the surface electromagnetic field and the subsurface electrical conductivity structure. The second level of functional relationship is between the set of governing physical parameters (e.g., seismic velocity) and a more fundamental set of model parameters represented by the major-element composition, pressure, water content, and temperature of the aggregate. Since this set of fundamental parameters (e.g., composition) controls the second set of governing physical parameters (e.g., shear velocity), they are commonly referred to as the primary and secondary parameters, respectively [*Bosch*, 1999; *Khan et al.*, 2007].

[63] The first level is the simplest and most widely used in conventional inversion methods. Typically, an appropriate physical theory (e.g., seismic wave propagation) is assumed and used to relate the secondary model parameters to the observations during the inversion. The final result is one or more sets of secondary physical parameters (i.e., Earth models), such as shear velocity or electrical conductivity, which exhibit an acceptable data fit. The second level of functional relationships is commonly ignored in inversion studies or treated as a posteriori independent (not self-consistent) corrections. Partly because of this, but also due to its intrinsic complexities (e.g., different compositions give the same seismic velocity), this functional level and its relationship with different geophysical observables in joint inversions are a less well-understood subject.

[64] In the following, we address both levels by discussing (i) the strengths and weaknesses of our choice of geophysical observables as well as their experimental uncertainties (section 4.2) and (ii) the intrinsic sensitivities of the secondary parameters Vs, Vp, bulk density, and ϵ to changes in the primary parameters in peridotitc assemblages (sections 4.3 and 4.4).

4.2. The Need for Multiple Observables

[65] The main purpose of inverting multiple geophysical observables is to minimize the range of acceptable models consistent with data. In other words, we aim to reduce the number of acceptable solutions to the inverse problem by taking into account more constraining data. It is therefore not only desirable but necessary that each piece of information (e.g., a new observable) newly added to the system has a different sensitivity to the model parameters of interest. If a new constraining dataset is added to the inversion, but its sensitivity to model parameters is similar to, or less than, that of the existent data, the inversion will not provide new information about the state of the system. In this work, we will combine information from gravity and geoid anomalies, seismic velocities, SHF, absolute elevation, and magnetotelluric data. We have purposely chosen these geophysical observables because they are differently sensitive to shallow/deep, thermal/compositional anomalies, which allows superior control over the lateral and vertical variations in the mantle's bulk properties. From a Bayesian point of view, what we want to achieve by including different datasets in a probabilistic inversion is to narrow the likelihood function $L(\mathbf{m})$ towards "good" values. However, the form of $L(\mathbf{m})$ is largely controlled by the form of $\rho(\mathbf{d})$, which in turn is controlled by the nature of the chosen geophysical observables, their associated uncertainties, and their intercorrelations (equations (7) and (9)). In this section, we discuss in detail the first two. The intercorrelations between uncertainties (both theoretical and observational) are addressed in paper II.

4.2.1. Gravity and Geoid Data

[66] Gravity and geoid anomalies are arguably the simplest and most commonly used geophysical observables for investigating lithospheric features [*Zeyen and Fernàndez*, 1994; *Zeyen et al.*, 2005; *Ebbing et al.*, 2006; *Jiménez-Munt et al.*, 2008; *Chappell and Kusznir*, 2008; *Kaban et al.*, 2010; *Watts*, 2001; *Jacoby and Smilde*, 2009, amongst others]. Unfortunately, given the $1/r^2$ dependence to the depth of the density anomaly, their sensitivity to typical lithospheric density anomalies decays to almost nil at depths $\gtrsim$50 km, except for large-scale anomalies with unusual density contrasts (e.g., continent-ocean boundary, Trans-European Suture Zone). Nevertheless, satellite-derived gravity anomalies offer one of the best spatial coverages of all available observables and can be used to put strong constraints on possible short-wavelength density distributions for the shallow lithosphere, especially when they are combined with seismic information [e.g., *Korenaga et al.*, 2001; *Roy et al.*, 2005]. For example, gravity anomalies are particularly suited to estimating the structure of the Moho and the elastic thickness of the lithosphere [cf. *Watts*, 2001; *Jacoby and Smilde*, 2009]. Their measurement uncertainties are typically low, varying between 2 and 10 mGal in global databases [*Sandwell and Smith*, 2009] to between 0.1 and 0.01 mGal in regional surveys.

[67] When the density anomaly is broad and deeper than around 50 km (e.g., within the SCLM), its signature in gravity anomalies becomes small and therefore, it is difficult to isolate the effects of the deep anomaly from those of other shallower anomalies, which dominate the signal. In this case, geoid anomalies (perturbations of the gravity potential) can prove a better constraint on the depth distribution of density due to their sensitivity to nonzero density moments [*Turcotte and Schubert*, 1982]. These characteristics make geoid anomalies better suited than gravity anomalies for constraining deep density anomalies, e.g., those arising from variations in the LAB (Appendix C). Uncertainties associated with recent geoid height models are extremely low, usually <5 cm accuracy down to 275 km half-wavelength [e.g., *Reigber et al.*, 2005]. Modelization errors (e.g., filtering and discretization) are therefore the largest source of uncertainty when fitting geoid heights (see paper II).

4.2.2. Surface Wave Data

[68] Phase velocity dispersion maps obtained from the combination of ANT with teleseismic surface wave tomography constitute one of the best sources of information for retrieving absolute Vs values in the lithosphere and

sublithospheric upper mantle [*Yang et al.*, 2008]. The main advantage of this method is that while ANT provides detailed information at short periods (shallow levels), teleseismic earthquake methods such as multiple-plane-wave tomography (MPWT) [*Yang et al.*, 2008] provide the complementary information at longer periods (deep levels). The ability to recover "good" values of Vs, however, depends on the uncertainties associated with the phase velocity dispersion maps generated by each method. In the case of ANT, robust estimations of the uncertainties in phase velocity maps can be obtained by the method of local Eikonal tomography [e.g., *Lin et al.*, 2009]. This method constructs a phase travel time map centered on each station of a seismic array by tracking phase travel times measured from cross-correlations of ambient noise between each station and all other stations within the seismic array. Each station-centered phase time map is then converted (separately) to a phase velocity map based on the Eikonal equation [e.g., *Shearer*, 1999]. The final phase velocity map is obtained by averaging all the individual phase velocity maps centered at different stations, and associated phase velocity uncertainties are estimated from the variations of multiple station-centered phase velocity maps. *Lin et al.* [2009] applied this approach to the EarthScope/US Array and showed that the period-averaged uncertainties associated with their dispersion maps typically average to <10 m/s for stations located in the middle of the array and ∼20 m/s for stations near the edges. Phase velocity uncertainties estimated in this way depend mainly on the quality of the travel time data and on the total number of stations in the seismic array.

[69] In the case of MPWT, uncertainties are estimated from the a posteriori model covariance matrix after solving the nonlinear least-squares problem [*Yang and Forsyth*, 2006].

$$\Delta m = \left(G^T C_{nn}^{-1} G + C_{mm}^{-1}\right)^{-1} \left(G^T C_{nn}^{-1} \Delta d - C_{mm}^{-1}[m - m_0]\right) \qquad (10)$$

where m_0 is the original staring model, m is the current model, Δm is the change relative to the current model, Δd is the difference between the observed and predicted data for the current model, G is the partial derivative of d with respect to perturbations of m, C_{nn} is data covariance matrix describing the data uncertainties, and C_{mm} is the prior model covariance matrix, which acts to damp or regularize the solution. A minimum length criterion is employed for damping by assigning a typical prior model variance of ∼0.2 km s^{-1} for phase velocity parameters to the diagonal term of C_{mm} and leaving all the off-diagonal terms to zero. For a study region with dense station coverage and sufficiently long duration of deployment, such as the US continent covered by the USArray, the choice of different damping values has only marginal effects on both phase velocity maps and uncertainties. In such cases, the uncertainties of data (i.e., surface wave phase and amplitude) are evaluated using an average data misfit for each event. Applying this method to the USArray data in Western USA, *Yang et al.* [2008] estimated period-averaged uncertainties of 10–15 m/s at stations near the center of the array. For other arrays/study regions, however, the effects of different damping parameters may not be marginal and thus, they need to be evaluated for that particular method and array (e.g., the choice of damping in MPWT could be gauged by comparing resulting phase velocity maps from MPWT at overlapped periods with those from Eikonal tomography, which does not require damping in obtaining phase velocity dispersion curves).

[70] With uncertainties of phase velocity maps both being able to be estimated for ANT and MPWT, one can then estimate uncertainties in Vs via Monte Carlo methods [e.g., *Yang et al.*, 2008]. In the case of the USArray data, the propagation of the uncertainties in the dispersion maps mentioned above results in uncertainties of 0.05–0.07 km/s in the absolute Vs structure of the mantle [*Yang et al.*, 2008]. It is worth noting that the above uncertainty estimates are valid only for the particular method discussed here, when using the dense USArray dataset. This exemplifies the ideal case for the sort of inversions described in this work. These uncertainties are not intended to be representative of the whole range of velocity models that would arise from the application of different methods. Specific uncertainties should be estimated from the particular method used to obtain the dispersion data rather than by comparing results from different methods (we do not use a mixture of results/data/methods).

4.2.3. Body Wave Data

[71] Body wave data have been used extensively to map the lithosphere and upper mantle structures for over three decades. Most regional body wave tomography use P-wave and/or S-wave travel time residuals that are calculated relative to a 1-D reference model to constrain Vp and/or Vs values of the lithosphere and sublithospheric upper mantle [e.g., *Rawlinson et al.*, 2006; *Shomali et al.*, 2006]. In a regional tomography, earthquakes are typically located outside the study region and therefore, in order to remove source path effects, the resulting Vp model is usually a model of velocity perturbation rather than an absolute velocities. This means that in order to obtain estimates of temperature and composition, one needs to first convert velocity anomalies into absolute velocities by superimposing the anomalies on the background reference model. However, using different reference models in body wave tomography commonly results in similar perturbation models; in other words, different reference models do not significantly affect the anomaly model. Thus, absolute velocity models based on regional body wave tomography only are not robust.

[72] In addition, due to differences in the methodologies and parameterizations/regulations used by different research groups, body wave anomaly models tend to be considerably different, even when using similar input data. For instance, *Becker* [2012] has recently compared several Vp models of western USA constructed from P-wave travel times recorded at the dense and broad USArray. This author found that, although the pattern of anomalies at scales ∼200 km is remarkably consistent between different models, significant differences in both amplitudes and small-scale patterns are the rule rather than the exception. Differences of several percent in the amplitudes of the anomalies are common between different models [*Becker*, 2012]. Such discrepancies are of the same order, if not larger, than those expected from large and moderate compositional and thermal anomalies, respectively. This illustrates an important limitation of body wave tomography as a direct proxy for compositional and thermal anomalies in the lithosphere.

[73] Within the present Bayesian framework, an attractive alternative that we discuss in paper II is to include

teleseismic arrival time residuals into the data vector **d** together with an additional operator $\mathbf{g}_{tt}$ used to compute synthetic travel time residuals [*Rawlinson and Sambridge*, 2004; *Rawlinson et al.*, 2006]. Although this adds a new set of uncertainties to the problem (those associated with observed and computed arrival times), it does guarantee that the absolute velocity model used to compute travel time residuals is simultaneously (and thermodynamically) consistent with dispersion data as well as with all other observables. This is, in itself, an important step forward for joint inversions. In this context, the uncertainties associated with arrival times are important to judge whether a model is acceptable or not under the framework of a Bayesian inversion. However, travel time uncertainties are notoriously hard to estimate, and thus most body wave tomography studies do not address the problem. Based on the few studies that attempted to estimate realistic uncertainties [e.g., *de Wit et al.*, 2012; *Gudmundsson et al.*, 1990; *Amaru et al.*, 2008], values of 0.5–1 s seem reasonable for large-scale studies. When dense local seismic networks are used instead, uncertainties associated with relative arrival time residuals can be, in average, less than 0.1 s [e.g., *Rawlinson et al.*, 2006].

4.2.4. Magnetotelluric Data

[74] Experimental uncertainty in magnetotelluric data comprises two types, random error and bias error. Random errors are well known and well understood, and modern jackknife-based methods give appropriate error estimates on the MT impedance tensor elements without assumptions about the distributions of the estimates [e.g., *Chave and Jones*, 1997; *Eisel and Egbert*, 2001; *Chave*, 2012]. High-quality data can usually be acquired with random errors of order 1% of the impedance values. In many places, however, the data errors are larger, mostly as a consequence of high noise disturbances (DC trains etc.). Also, long period signals can be lower, as signal strength is directly related to the 11-year sunspot cycle.

[75] Far more difficult to quantify are bias errors that are caused by distortion effects [e.g., *Jones*, 2012]. These take two forms, either galvanic distortion that can lead particularly to errors in primarily the magnitudes of the MT impedances or inadequate dimensionality assumption, i.e., interpreting 2-D data using 1-D methods or 3-D data using 2-D (or 1-D) methods. For the latter, there are dimensionality tests that can be performed, and the one in most current use is the Groom-Bailey approach [*Groom and Bailey*, 1989], particularly the multisite, multifrequency code of *McNeice and Jones* [2001]. For the former, there are approaches in use to control the indeterminable part of distortion, the so-called "static shifts" [*Jones*, 1988]. Generally, for high-quality MT data that are appropriately treated, experimental uncertainty is of order some 1–2% of the impedance values.

[76] The mapping from experimental errors into model errors is difficult and fraught with high potential for misunderstanding. Although there exists a uniqueness theorem in 1-D and one of the 2-D modes for perfect MT data at all frequencies [*Bailey*, 1970], for real data with error, one must be cognizant of the issues. The functional relationship between conductivity and observed response is highly nonlinear, and again, there are random errors and bias errors. Random errors can be quantified through linearized approaches, such as that of *Schwalenberg et al.* [2002] in two dimensions (2-D). Bias errors are far more difficult to quantify and relate mainly to the insensitivity of inductive methods to the resistivity of a resistive region, where "resistive" and "conductive" are relative terms. For example, the resistivity of the uppermost mantle directly below the crust is typically impossible to determine accurately due to the presence of conducting material in the lower crust [see, e.g., *Jones* 1999, figure 3]. Only in cases where the crust is resistive for its entire depth extent is it possible to determine the absolute resistivity of the uppermost mantle [e.g., *Jones and Ferguson*, 2001; *Ledo et al.*, 2004]; otherwise, a minimum bound can be set for the resistivity, but not a maximum bound. Regularization errors will be discussed in paper II.

4.2.5. Absolute Elevation

[77] Observational uncertainties associated with elevation are low, amounting to $\lesssim$15 m in high-resolution (30 arc s resolution) global databases [*Becker et al.*, 2009]. In our inversions, however, the area of the individual columns is sufficiently large ($\sim$2500–10,000 km^2) to include significant local variations in elevation that need to be averaged to a single value with a representative uncertainty. We do this by calculating the mean and standard deviation of the individual data points within each column. In most cases, the standard deviations so obtained are $\lesssim$150 m.

4.2.6. Surface Heat Flow

[78] Surface heat flow measurements are expensive, particularly in continents, and therefore they are scarce and heterogeneously distributed [e.g., Davies and Davies, 2010]. In addition, SHF values are typically dominated by the heat production of the crust and are significantly affected by shallow advection processes; their sensitivity to deep mantle thermal anomalies is strongly diminished when these are located at depths >180 km [cf. *Jaupart and Mareschal*, 2011]. For these reasons, lithospheric/sublithospheric models based purely on SHF data are not considered to be reliable. Despite these limitations, SHF nevertheless provides some constraints, albeit weak, and can be a useful "secondary" observable when dealing with the mantle thermal structure. By secondary we mean that, although the relative weight assigned to SHF during the inversion is low in comparison with other observables (e.g., seismic waves), any acceptable model of the lithosphere/sublithosphric upper mantle must be consistent with SHF data as well.

[79] Typical uncertainties associated with SHF measurements in continents amount to $\pm$5–10 mW m^{-2} [e.g., *Powell et al.*, 1988], which is equivalent to a depth change in the LAB of $\sim$50 km (if the LAB is defined as an isotherm, e.g., 1300°C). However, this equivalency is strictly valid only if the LAB change is confined to a depth range between $\sim$60 and 180 km. At 250 km depth, an identical change in depth translates into a SHF change of only 5–8 mW m^{-2}.

4.3. Dependence of Physical Parameters on Major-Element Composition

4.3.1. An Illustrative Example

[80] Let us assume that we have laboratory measurements of the (secondary) parameters Vs, Vp, electrical conductivity ϵ, and bulk density for a peridotite sample at P = 3 GPa and T = 900 °C (assume that Vs and Vp are high-frequency, unrelaxed, velocities). Our task is to retrieve the true major-element composition of the sample by exploring the entire compositional space with a Monte Carlo method and

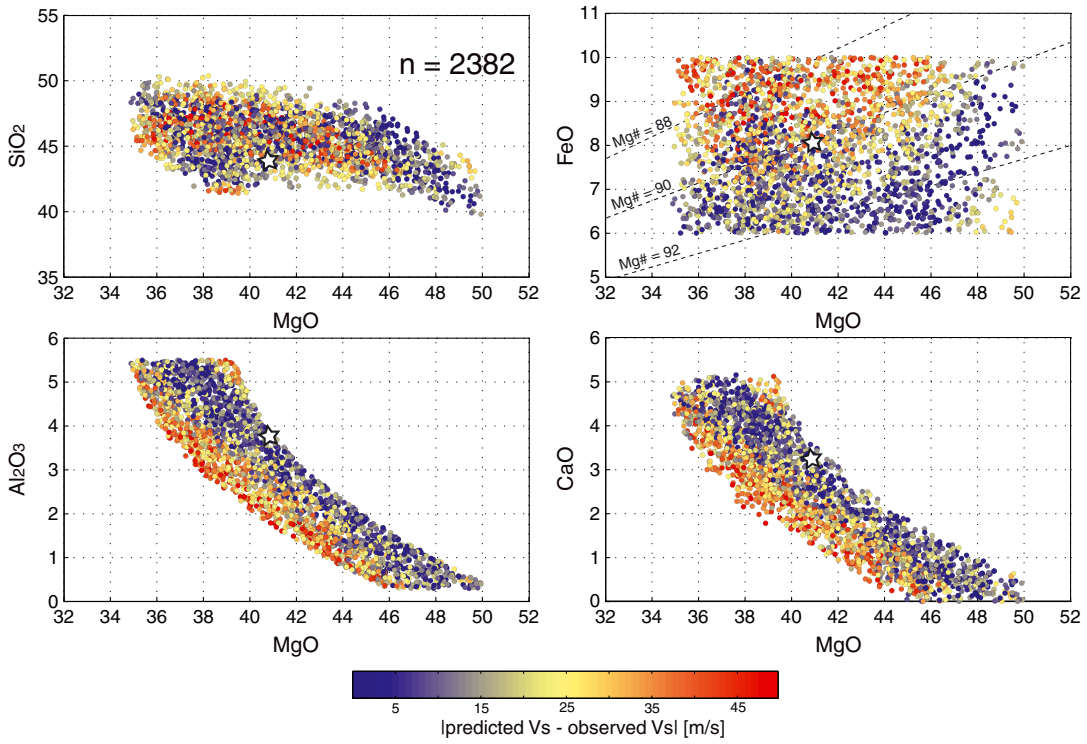

Figure 6. Ensemble of 2382 acceptable compositions from a total random population of 2500 samples. The only constraining parameter is the Vs velocity. The true (target) composition is indicated by the white star (SiO_2 = 44.03, Al_2O_3 = 3.81, FeO = 8.08, and MgO = 40.82, CaO = 3.25) and the corresponding target Vs velocity is 4.634 km s^{-1} (calculated at T = 900 °C, P = 3 GPa). The color scale represents the misfit in absolute values. The sampling is performed following the steps explained in the text and truncating the samples at the 95% confidence limits.

comparing our predictions to the observed parameters. Predicted values of Vp, Vs, ϵ, and bulk density for all tested compositions are obtained by solving the Gibbs energy minimization problem (section 3.1). To make a (much simplified) comparison with real-case scenarios easier, further assume that the measurements have associated uncertainties in Vs and Vp comparable to those from dense surface wave and refraction studies ($\pm$52 and $\pm$82 m s^{-1} for Vs and Vp, respectively). We warn the reader that these uncertainties, although realistic, are strictly valid for the present illustrative example only. More appropriate values (particularly for Vp and dispersion curves) will be used in a real 3-D inversion (paper II).

[81] We generate sets of 2500 random compositional samples each, using the method described in section 2.3 (this number is sufficient to sample well the entire compositional field indicated by real samples; Figure 2). During each simulation, we save a subset containing the samples that fit the data within their defined uncertainties. This subset then constitutes an ensemble of *acceptable samples*. Figure 6 shows the result of one such simulations in which Vs is the only constraining parameter. All samples in this subset fit the true Vs value within $\pm$52 m s^{-1} (the assumed uncertainty). Note that the assumed uncertainty is close to the low end of representative uncertainty values in high-resolution surface wave studies (section 4.2.2), and thus, this example represents the best possible scenario. Even when the uncertainty is reduced by a factor of two (unrealistically good), the resulting subset of samples consistent with the data still spreads over a large compositional range. This simple exercise demonstrates that Vs alone defines neither the composition of our synthetic sample nor the fine compositional structure of the Earth's upper mantle; it only suggests that a peridotitic composition *sensu lato* is compatible with the observed Vs value.

[82] When Vp is used as the only constraint, the subset of acceptable samples is smaller than when using Vs, but the acceptable compositional range remains large (Figure 7). In this case, the samples of this subset fit the true Vp value within $\pm$82 m s^{-1}, which is again close to the low end of typical uncertainties in refraction studies. The reason for the reduction on the number of acceptable samples when using Vp instead of Vs is mainly due to the disappearance of the "low-Al_2O_3" samples (yellow-red dots in Figure 6). This is because, at equal MgO contents, the bulk modulus of the assemblage is more sensitive to changes in bulk Al_2O_3 (i.e., garnet mode) than the shear modulus. Therefore, the acceptable Al_2O_3 range for samples with an identical MgO content is narrower in Figure 7. However, as in the Vs case, the compositional range allowed by Vp is large enough to include most of the natural variability (Figure 2). Note the two regions of low misfit (blue dots) at high and low MgO contents. The low-residual samples at the high-Mg end are harzburgites (opx + ol) and dunites (mostly ol) while those at low-Mg end are lherzolites (cpx + opx + ol + gte). When

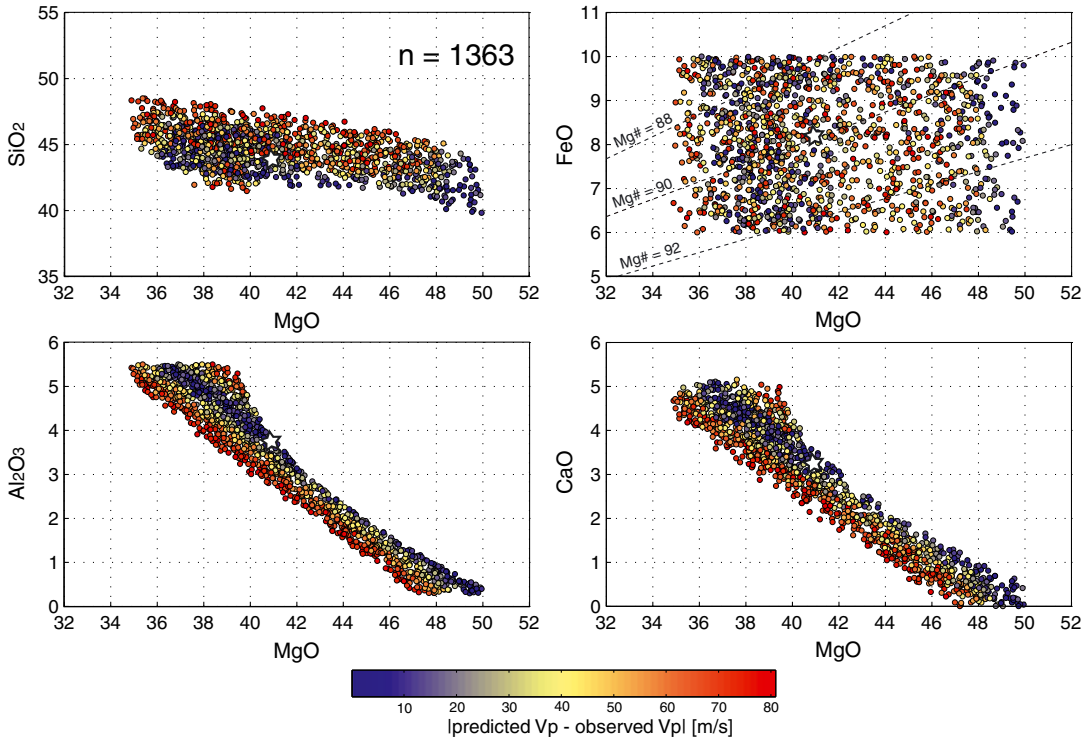

Figure 7. Ensemble of 1363 acceptable compositions from a total random population of 2500 samples. The only constraining parameter is the Vp velocity. The true (target) composition is the same as in Figure 6 (white star) and the corresponding target Vp velocity is 8.185 km s^{-1} (calculated at T = 900 °C, P = 3 GPa). The color scale represents the misfit in absolute values. Sampling method as in Figure 6.

larger uncertainties are considered (±120 m s^{-1}), the subset of acceptable samples is larger, but the two regions of low misfit at high and low MgO contents remain. In the ideal case of small uncertainty in the observed Vp value (±10 m s^{-1}), the diagram would show two separate clusters of acceptable samples, and independent information would still be needed to decide on the composition of the sam ple. This two-branched pattern in Vp has been recognized before [*Afonso and Schutt*, 2012] and reflects the competition between modal (phase abundances) and chemical (composition of the phases) effects in peridotites as their Al_2O_3 and CaO contents decrease. As expected, fitting Vp and Vs simultaneously (or their ratio) produces similar results as those in Figure 7, and therefore, we do not include an additional figure.

[83] At first glance, these results seem to be at odds with the strong correlations between Vp/Vs and Mg% found in several previous studies [e.g., *Lee*, 2003; *Speziale et al.*, 2005; *Afonso et al.*, 2010]. However, although the correlations are a robust result, the actual application of them to infer the Mg% of mantle domains is hampered by the unrealistically low uncertainties required for Vp, Vs, and/or ρ. When realistic uncertainties associated with these properties are considered (e.g., ±0.02 for Vp/Vs ratio), the range of possible Mg% as given by the above correlations becomes large enough to cover most of the natural range in peridotites [compare with Figure 2 in *Afonso et al.*, 2010]. This is precisely what Figures 6 and 7 highlight; the contradictions are therefore only apparent.

[84] Assigning uncertainties to density data in the upper mantle is more problematic, since traditional geophysical methods are weakly sensitive to absolute density values at small scales (<250 km). For our present (illustrative) purposes, an objective uncertainty can be estimated based on the discrepancies between predictions from different thermodynamic [*Holland and Powell*, 1998 (revised 2002); *Stixrude and Lithgow-Bertelloni*, 2011], hybrid [*Afonso et al.*, 2008], and mineral physics methods [*Schutt and Lesher*, 2006] for identical compositions. We have compared predictions from the methods of *Schutt and Lesher* [2006], *Afonso et al.* [2008], and *Stixrude and Lithgow-Bertelloni*, [2011] for identical samples and found that their discrepancies amount to <1% for conditions pertaining to the upper mantle [see also *Afonso and Schutt*, 2012]. With these estimates, a simulation using density as the only constraint generates the subset of acceptable samples shown in Figure 8. Since bulk density is the bulk property that correlates best with Mg#, the compositional range along the MgO and FeO axes has been reduced compared with those from Vs or Vp. Also, at identical MgO contents, the range in SiO_2 content has been reduced. This is due to the significant effect of the low-density phase Opx (which is controlled by the SiO_2 content of the sample) on bulk density. Despite these improvements, the compositional range still is too large to provide a definite composition for our sample.

[85] Electrical conductivity alone does not represent any improvement with respect to the other parameters (Figure 9),

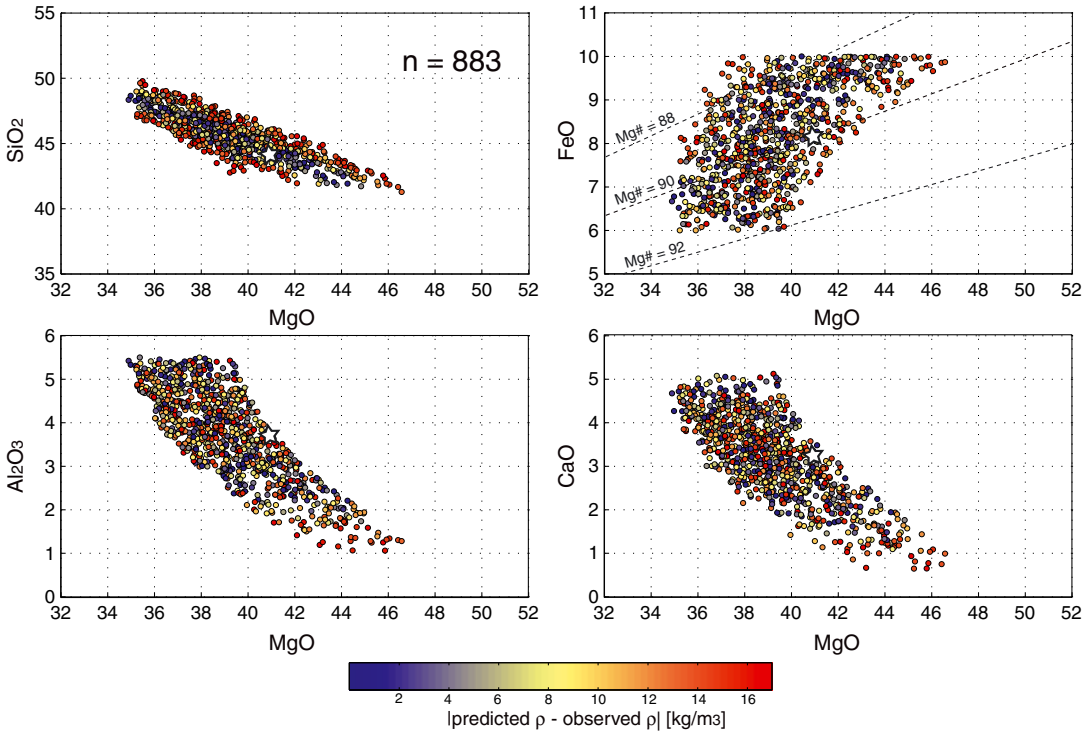

Figure 8. Ensemble of 883 acceptable compositions from a total random population of 2500 samples. The only constraining parameter is the bulk density. The true (target) composition is the same as in Figure 6 (white star) and the corresponding target density 3378.79 kg m^{-3} (calculated at T = 900 °C, P = 3 GPa). The color scale represents the misfit in absolute values. Sampling method as in Figure 6.

except that there is more clearly defined region of low residuals. This is a consequence of the large effect that garnet has on the bulk conductivity of peridotites (garnet conductivity is typically 1–2 orders of magnitude greater than that of other phases). Thus, the "banding" depicted by the residual in the SiO_2-MgO panel follows closely the original banding in garnet content. Interestingly, the region of low residuals seems to be equally spread around the true values of Al_2O_3, FeO, and CaO but preferentially displaced towards lower MgO and higher SiO_2 values. This apparently odd feature is the result of competing modal effects and can be understood as follows: reducing MgO and increasing SiO_2 results in assemblages with larger Opx/Ol, Cpx/Ol, and Gt/Ol ratios. Orthopyroxene and clinopyroxene have electrical conductivities slightly lower than, or comparable to, that of olivine [*Fullea et al.*, 2011]. Therefore, while an increase in Opx + Cpx/Ol reduces the bulk conductivity of the rock, increasing the Gt/Ol ratio has an opposite and stronger effect. The overall result is that small increases in the Gt/Ol ratio can compensate for larger increases in the Opx/Ol ratio. This is a somewhat unfortunate characteristic of electrical conductivity that systematically biases the location of regions with low residuals to lower MgO and higher SiO_2 values than those in the target sample.

[86] The obvious next step is to simultaneously fit Vs, Vp, ϵ and bulk density within their uncertainties in an attempt to constrain the range of acceptable samples as much as the data allow. The results of such simulation are shown in Figure 10. The residual in this case is simply defined as

$$residual = \frac{|\mathrm{Vs}(\mathbf{m}) - \mathrm{Vs}_{\mathrm{obs}}|}{\sigma_{\mathrm{Vs}}} + \frac{|\mathrm{Vp}(\mathbf{m}) - \mathrm{Vp}_{\mathrm{obs}}|}{\sigma_{\mathrm{Vp}}} + \frac{|\rho(\mathbf{m}) - \rho_{\mathrm{obs}}|}{\sigma_{\rho}} + \frac{|\epsilon(\mathbf{m}) - \epsilon_{\mathrm{obs}}|}{\sigma_{\epsilon}} \quad (11)$$

where $\mathbf{m}$ is the vector of compositions, Vs($\mathbf{m}$), Vp($\mathbf{m}$), $\rho(\mathbf{m})$, and $\epsilon(\mathbf{m})$ the predicted values, $\mathrm{Vs}_{\mathrm{obs}}$, $\mathrm{Vp}_{\mathrm{obs}}$, ρ_{obs}, and ϵ_{obs} the observed values, and σ_{Vs}, σ_{Vp}, σ_{ρ}, and σ_{ϵ} the respective mean deviations (σ_{Vs} = 52 m s^{-1}, σ_{Vp} = 82 m s^{-1}, σ_{ρ} = 20 kg m^{-3}, σ_{ϵ} = 0.25 $\log_{10}$ S m^{-1}). As expected, Figure 10 shows a much more restricted compositional range than the ones obtained using Vs, Vp, ϵ, and density separately. Only 22% of the total number of random samples generated met the imposed fitting criteria. Although this result is encouraging, we still would have difficulties in choosing a definite composition for the sample at hand, even if we only needed to define its Mg# approximately. Even samples with residuals <1 do not cluster around definite values but rather follow a trend in the compositional space. A more thorough search in compositional space reveals an even clearer but identical trend of acceptable samples (Figures D2a–D2d in Appendix D). It is important to identify the reasons behind this behavior since (i) this trend of acceptable samples seems at odds with the common idea that different Mg# represent signif-

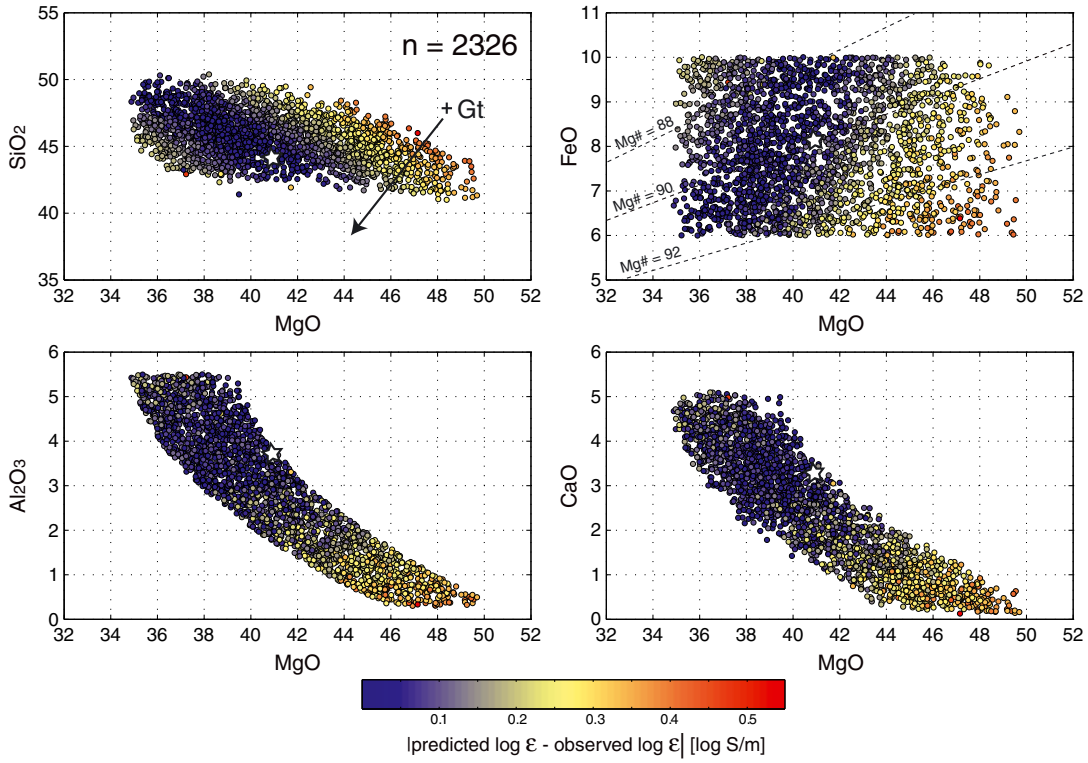

Figure 9. Ensemble of 2326 acceptable compositions from a total random population of 2500 samples. The only constraining data is the bulk electrical conductivity. The true (target) composition is the same as in Figure 6 (white star) and the corresponding target electrical conductivity is $\log_{10} \epsilon = -3.9163$ $\left[\log_{10} \text{ S m}^{-1}\right]$ (calculated at T = 900 °C, P = 3 GPa). The black arrow indicates the direction of increasing garnet content in the samples. The color scale represents the misfit in absolute values. Sampling method as in Figure 6.

icantly different physical properties and (ii) it complicates any inversion procedure within the compositional space.

[87] The trend of low misfit samples (blue dots), running roughly from high-Mg/low-Al/high-Fe to low-Mg/high-Al/low-Fe, is the result of a combination of modal and compositional effects. The high-Mg/low-Al/high-Fe samples are basically harzburgites with anomalously high Al and Fe contents, while the low-Mg/high-Al/low-Fe samples are lherzolites with anomalously low Fe contents (compared with natural samples in Figure 2). Over 95% of high-Mg peridotites in our database are depleted rocks with low contents of Al and Ca (Figure 2), which typically results in low-density rocks with higher Vs and Vp velocities than their fertile counterparts. In the present case, however, the anomalously high FeO contents of the harzburgites promote the stabilization of denser olivine (Fa-rich olivine) with lower Vp and Vs velocities than normal. Additionally, the relatively high Al contents of these samples result in higher than normal contents of the dense phase garnet. The final result is that the FeO and Al_2O_3 effects counterbalance the high-Mg effect, and thus the physical properties of the harzburgitic samples resemble those of more fertile lherzolites. This is the reason why the field of acceptable samples is extended towards higher Mg# in Figure 10. The cause of the extension towards lower Mg# can be understood on similar grounds. The anomalously low FeO contents in the lherzolitic samples of Figure 10 result in samples with higher Vs and Vp and lower densities than average natural lherzolites (low-Fe end members are typically less dense and have higher velocities). Importantly, note that although the Al_2O_3 content is relatively high, this does not translate into significantly larger amounts of denser garnet due to a "buffer" effect by the pyroxenes, which can accommodate larger amounts of Al_2O_3 at low pressures [e.g., *Perkins and Newton*, 1980]. This buffer effect is discussed further below.

[88] The existence of this trend complicates any attempt to constrain the composition of the sample, since all samples are identical in terms of their relevant physical properties (Table 2). This hitherto described problem represents a serious challenge for any inversion scheme attempting to provide estimates of the compositional structure of the upper mantle. Interestingly, this modal-compositional effect is significantly minimized as the pressure increases, mainly due to the disappearance of the buffer effect provided by pyroxenes (Appendix D). As mentioned above, the capacity of pyroxenes to accommodate Al_2O_3 in their structure decreases with pressure [*Perkins and Newton*, 1980], which in turn amplifies the dependence of modal garnet on bulk Al_2O_3 content. At the same time, the majoritic component of opx becomes more soluble in garnet as pressure increases [e.g., *Irifune and Ringwood*, 1993], thus increasing modal gt/opx. All this results in that even relatively small changes in Al_2O_3 content at high pressures (P $\gtrsim$10 GPa) can translate into

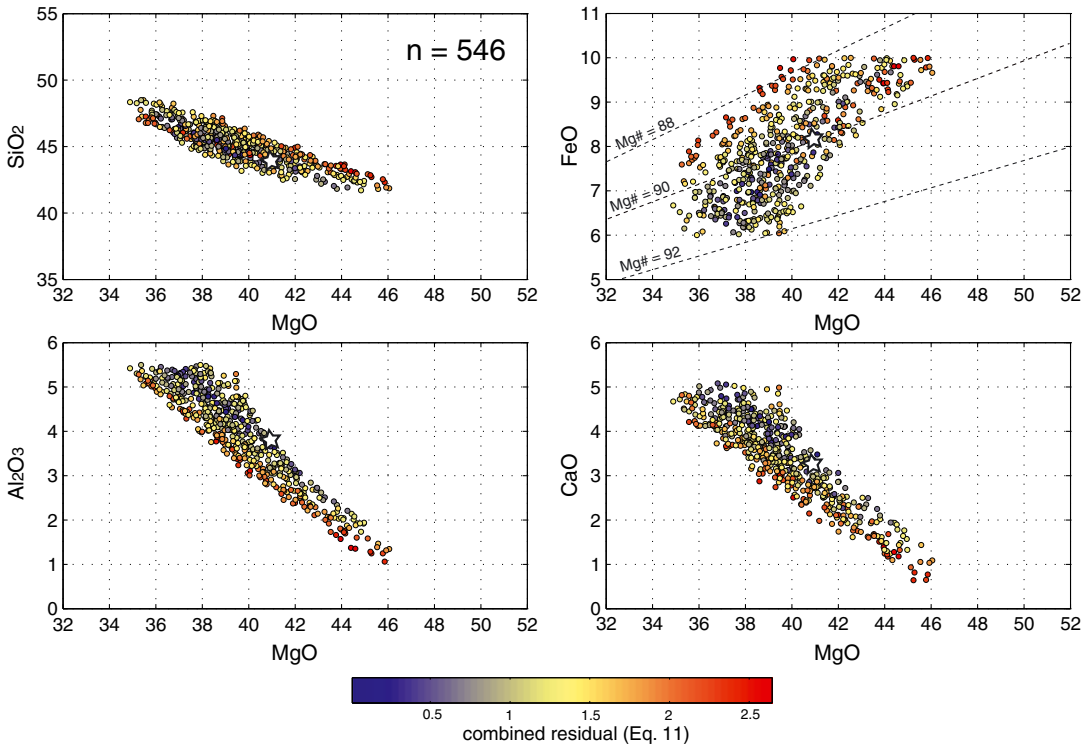

Figure 10. Ensemble of 546 acceptable compositions from a total random population of 2500 samples. These acceptable samples simultaneously fit Vs, Vp, electrical conductivity, and bulk density constraints (within uncertainties). True (target) composition and P-T conditions as in Figure 6, and the corresponding Vp, Vs, ϵ, and density as in Figures 6–9. The color scale represents the combined residual explained in the text.

significant variations in the garnet mode. Since garnet is the densest, fastest, and most conductive phase in the rock, modest variations in its mode significantly affect the physical properties of the rock. Because this modal effect is more important than that exerted by modest variations in FeO content, the dependence of bulk density, Vs, Vp, and electric conductivity on compositional variations is effectively augmented at high pressures and thus the trend seen in Figure 10 is much reduced (Appendix D). In summary, constraining the composition of an upper mantle peridotite using only its physical properties is easier at depths $\gtrsim$300 km. Thus, the depth range over which constraining compositional anomalies with geophysical observables is less robust encompasses most of the lithospheric mantle. Inversion schemes that include a compositional space for the lithosphere should explicitly consider this matter.

4.3.2. A Simple Bayesian Strategy

[89] To this point, it would seem that the combination of the four observations fails to define a good estimate of the sample's composition, even when the experimental

Table 2. (a) Volumetric Proportions, Phase Compositions, and Physical Properties of a Peridotite Sample With Bulk Composition SiO_2 = 45.59, Al_2O_3 = 4.82, FeO = 7.0, MgO = 38.01, and CaO = 4.93. (b) Volumetric Proportions, Phase Compositions, and Physical Properties of a Peridotite Sample With Bulk Composition SiO_2 = 42.27, Al_2O_3 = 2.50, FeO = 9.84, MgO = 45.00, and CaO = 0.57[a]

(a) Phases	vol%	SiO_2	Al_2O_3	FeO	MgO	CaO	ρ [kg m^{-3}]	Vs [km s^{-1}]	Vp [km s^{-1}]
Ol	54.65	41.81	0.00	*8.13*	50.68	0.00	*3324.0*	*4.65*	*8.20*
Opx	10.65	57.50	0.95	6.45	34.59	0.51	3300.3	4.53	7.73
Cpx	17.26	54.82	0.89	1.36	18.36	24.57	3296.3	4.36	7.76
Gt	17.43	42.52	23.95	*8.96*	20.76	3.81	*3688.5*	4.94	8.89
Aggregate	x	45.59	4.82	7.0	38.01	4.93	**3380.2**	**4.63**	**8.18**
(b) Phases	vol%	SiO_2	Al_2O_3	FeO	MgO	CaO	ρ [kg m^{-3}]	Vs [km s^{-1}]	Vp [km s^{-1}]
Ol	83.04	40.83	0.00	*9.99*	49.17	0.00	*3348.3*	*4.61*	*8.15*
Opx	7.11	57.26	0.89	7.49	33.87	0.47	3313.3	4.51	7.70
Cpx	0.55	54.74	0.88	1.65	18.12	24.59	3299.9	4.36	7.76
Gt	9.30	42.21	23.77	*10.47*	19.59	3.95	*3711.8*	4.93	8.86
Aggregate	x	42.27	2.50	9.84	45.00	0.57	**3379.3**	**4.63**	**8.18**

[a]Calculations were performed with Perple_X [*Connolly*, 2009] at P = 3 GPa, T = 900 °C. The thermodynamic formalism and database are from *Stixrude and Lithgow-Bertelloni* [2011].

uncertainties are low. This may not be necessarily the case if we set up the problem as a probabilistic inversion exercise and take into account all the information gained about the problem by the experiments in previous sections. As a provisional solution to the current problem, we propose the following general strategy.

[90] (1) The prior for compositional parameters $\rho(\mathbf{m})$ is based on the data provided by the dataset of exhumed samples (Figure 2). It is sampled as described in section 2.3, now explicitly including in $\rho(\mathbf{m})$ the Gaussian distributions for CaO and MgO associated with each Al_2O_3 bin (Figures 3 and 4). Note that $\rho(\mathbf{m})$ represents a true prior, as it is independent of any geophysical data.

[91] (2) Assign a PDF for the relevant operators solving the forward problem; equation (9) represents an appropriate option.

[92] (3) Define the likelihood function $L(\mathbf{m})$ of the problem. Based on the discussions in previous sections, an appropriate option is [*Tarantola*, 2005]

$$L(\mathbf{m}) = \int \frac{\rho(\mathbf{d})\,\theta(\mathbf{d} \mid \mathbf{m})}{\mu(\mathbf{d})}\,\mathrm{d}\mathbf{d} = k\left(-\frac{1}{2}(\mathbf{g}(\mathbf{m}) - \mathbf{d}_{\mathrm{obs}})^T C_D^{-1}(g(\mathbf{m}) - \mathbf{d}_{\mathrm{obs}})\right) \qquad (12)$$

where k is a constant, d_{obs} is the observed data vector (i.e., observed values of Vp, Vs, and ρ), and C_D is the covariance matrix that incorporates both theoretical and data uncertainties. The second equality in equation (12) implies Gaussian PDFs for both $\mu(\mathbf{d})$ and $\theta(\mathbf{d} \mid \mathbf{m})$ (the analytical solution of the integral in equation (12) can be found in *Mosegaard and Tarantola* [2002]). For this simple example, it suffices to assume a diagonal C_D (i.e., uncorrelated uncertainties). The computation of the full-rank covariance matrix for the 3-D inversion problem is discussed in paper II.

[93] (4) Substitute the above PDFs into equation (6) and solve for $\sigma(\mathbf{m})$. Since there is no closed-form mathematical expressions for either $\rho(\mathbf{m})$ or $\sigma(\mathbf{m})$, we use a Markov Chain Monte Carlo (MCMC) method to sample these PDFs. A thorough discussion of MCMC methods is beyond the scope of this paper, and we refer the reader to *Gilks et al.* [1996] and *Brooks et al.* [2011] for details. Here, it suffices to state that the algorithm samples the posterior PDF by iteratively proposing independent samples of the prior $\rho(\mathbf{m})$ and evaluating their likelihoods. The proposed sample $\mathbf{m}_{\mathrm{new}}$ are accepted as samples of the posterior with a probability $P = \min[1, L(\mathbf{m}_{\mathrm{new}})/L(\mathbf{m}_{\mathrm{prev}})]$, where $\mathbf{m}_{\mathrm{prev}}$ is the likelihood of the last accepted sample.

[94] We emphasize that the only (loose) constraint in this scheme is that the sampling of the prior is restricted to a space defined by our large database of natural samples from different tectonic settings (Figure 2). This contrasts with the more common and restrictive assumptions of (i) models based on limited, local xenolith samples [e.g., *Fernàndez et al.*, 2010; *Fullea et al.*, 2010], (ii) compositional regionalizations based on assumed crustal age-composition relationships [e.g., *Cammarano et al.*, 2011], and (iii) small compositional ranges for the upper mantle [e.g., *Khan et al.*, 2011a] . This is important for several reasons. First, there is abundant evidence that the relationship between crustal age versus mantle composition does not apply worldwide [e.g., *Griffin et al.*, 1998; *Griffin et al.*, 2009]. Second, local xenolith suites may not

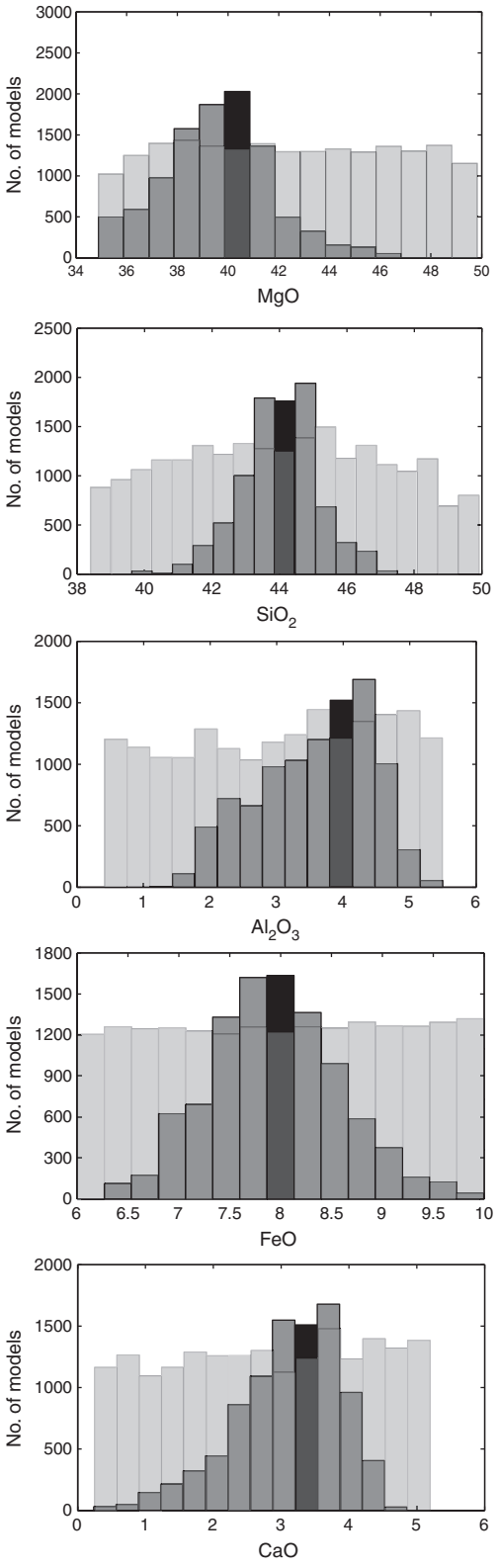

Figure 11. Prior (transparent) and posterior (dark gray) histograms (i.e., marginal distributions) from an MCMC simulation performed following the steps explained in the text. The bin containing the true value is colored black. In all cases, the histograms have been significantly narrowed towards the true value.

be representative of the lithospheric mantle as a whole [e.g., *Afonso et al.*, 2008; *Griffin et al.*, 2009]. Third, and perhaps more important, most geophysical observables are not strongly sensitive to major-oxide compositional anomalies (section 4.3.1), and therefore, restrictive priors can significantly condition the final result of the inversion (Figure 1).

[95] The results from an MCMC simulation using the steps described above are shown in Figure 11 for the same composition and P-T conditions as in Figures 6–10. The prior and posterior marginal distributions are depicted as histograms computed from the full posterior ensemble. The acceptance rate of the MCMC algorithm was about 30%, and therefore, the prior ensemble is ∼70% larger than the posterior. Note that the region of highest probability successfully encloses the true solution and defines a Mg# within ∼ ±0.5 units. Changing the target (true) composition to more extreme compositions does not affect the general conclusion, and our method still is able to retrieve a satisfactory estimate of the true composition (Appendix D). Regardless of these results, the application of this approach to 3-D inversion problems with real geophysical data, as well as its capacity to recover robust estimates of the thermochemical structure of the Earth's upper mantle, requires a number of additional considerations, both conceptual and computational. These will be thoroughly addressed in paper II.

[96] The type of strategy described here is common practice in full Bayesian analyses, where only information that is entirely independent of data is accepted as prior [*Tarantola*, 2005]. However, other "objective" information could be implemented by reformulating the problem as a hierarchical or empirical Bayes problem [*Carlin and Louis*, 2000; *Efron*, 2010]. In particular, in all of our tests, the resulting ensemble of acceptable samples obtained through a simple Monte Carlo search tends to be evenly distributed around the true value (e.g., Figure 10). This is not surprising, as the fitting properties of a particular sample are expected to decrease the further it is from the true value. Under certain circumstances, this information could be treated as hyperprior information about the problem and let the data inform the actual prior of compositional parameters. For example, the hyperparameters could be the mean vector and covariance matrix defining the prior $\rho(\mathbf{m})$. Alternatively, a reduced data vector could be used in a "first approximation" step to obtain hyperparameters that would define the priors to use when incorporating all available data in the Bayesian analysis. Such approach, in which the prior is informed by all or part of the data (and therefore not a true prior in the strict Bayesian sense), has proven to be particularly useful in geophysical inversions [e.g., *Butcher et al.*, 1991; *Gouveia and Scales*, 1998; *Scales and Tenorio*, 2001; *Oh and Kwon*, 2001; *Malinverno and Briggs*, 2004; *Woodbury and Ferguson*, 2006], but the actual procedure depends on both the problem and the type of information to be retrieved. Similar grounds applied to our full 3-D inversion scheme will be discussed in paper II [*Afonso et al.*, this issue].

4.3.3. Linear ρ-Velocity Correlations for Peridotites

[97] A related issue relevant to this section, in which differences in major-element composition can potentially affect Vp-density or Vs-density joint inversions, is the validity of

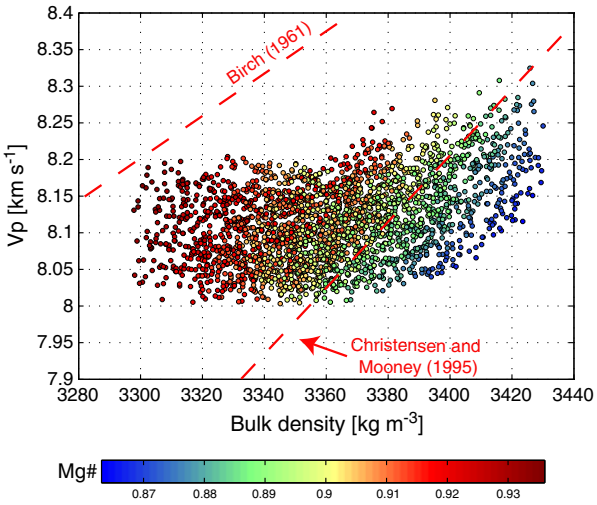

Figure 12. Vp-bulk density plot for 2500 random peridotite samples from a Monte Carlo simulation at P = 3 GPa and T = 900 °C. These samples cover >95% of the entire compositional range as depicted in Figure 2. The dashed lines are the empirical linear relations for ultramafic rocks from *Birch* [1961] and *Christensen and Mooney* [1995]. The Mg# of each sample is indicated by the color scale.

the so-called Birch's law [*Birch*, 1961] for mantle samples at lithospheric conditions. Similarly to what is assumed at crustal levels, joint inversions typically assume that there is a linear correlation between Vp and bulk densities at sub-Moho depths [e.g., *Nielsen and Jacobsen*, 2000; *Bailey et al.*, 2012]. Figure 12 shows the result of a Monte Carlo simulation in which 2500 random samples have been generated within the compositional bounds given by Figure 2. Bulk density and Vp of these samples were calculated at P = 3 GPa and T = 900 °C. We also include in this figure the predictions from the original fit of Birch for mantle rocks [*Birch*, 1961] at pressures up to 1 GPa and the more recent estimation of *Christensen and Mooney* [1995] for sub-Moho depths. As expected from the different pressure ranges, the original fit is well outside the predicted values. That of *Christensen and Mooney* [1995], on the other hand, passes through the ensemble, almost parallel to the field of "fertile" lherzolites (i.e., samples with Mg# ∼0.89). This suggests that the linear parametrization of *Christensen and Mooney* [1995] is a reasonable approximation only for relatively fertile peridotites. Samples with higher Mg#, i.e., from typical depleted cratonic upper lithospheric mantle, depart significantly from the linear fit, resulting in differences up to ∼80 kg m^{-3} in the predicted density. This value is of similar order to that resulting from a change in lithology (Appendix A). For the SCLM beneath Phanerozoic terranes, the "fertile" xenoliths may represent a reasonable approximation to the composition. However, beneath cratons and Proterozoic terrains, such fertile rock types are probably in a minority and concentrated along specific zones that have experienced repeated refertilization [*Griffin et al.*, 2009; *O'Reilly and Griffin*, 2012]. Therefore, caution should be exerted when applying generalized linear fits in Vp-density joint inversions.

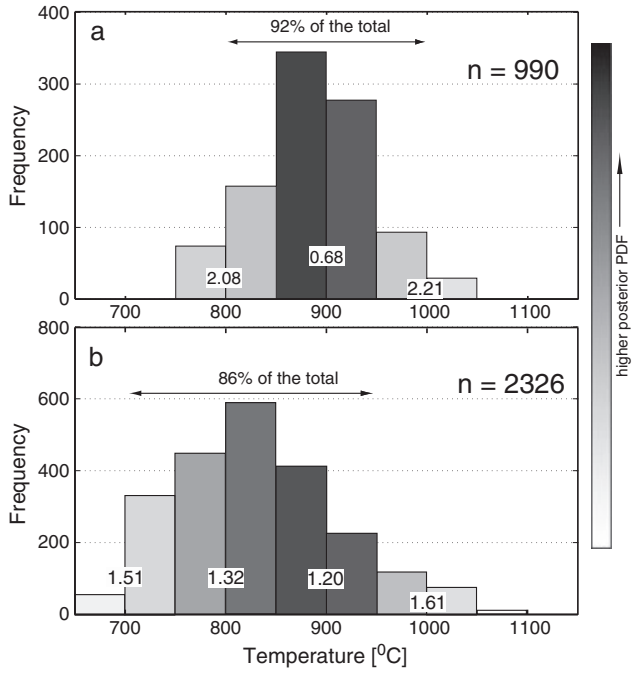

Figure 13. Histogram of 990 samples that fit Vp, Vs, bulk density, and electrical conductivity within uncertainties. Note that more than 92% of these samples are found within the range 800 < T < 1000°C. (b) as in (a) but excluding electrical conductivity from the constraining parameters. The color scale denotes values of the normalized posterior PDF. Numbers between two temperature bins are the average residuals (as defined in equation (11)) for the two adjacent bins. See text for details.

4.4. Dependence of Physical Parameters on Temperature

[98] The effect of temperature on anharmonic physical properties of upper mantle minerals is generally better understood than the compositional effects [cf. *Ahrens*, 1995, *Anderson*, 1995; *Rubie et al.*, 2004; *Yoshino*, 2010; *Price*, 2009; *Jones et al.*, 2012]. Therefore, we do not attempt to address this subject here; the interested reader can find detailed reviews in the references given above. More relevant to us is the minimum range of temperatures that our observables can constrain when compositional effects are simultaneously included in the inversion. In Bayesian terms, we would like to know how broad the likelihood function is (and therefore the posterior PDF) with respect to temperature. An instructive and simple way to achieve this is to add temperature to our vector of model parameters **m** and run Monte Carlo simulations to find acceptable ensembles that fit the data within uncertainties. The strategy here is first to generate 2500 random compositional samples in the same way as in the previous section and then to calculate their physical properties for 40 different temperature bins of 25°C each. This provides a sufficiently smooth sampling of temperature from 500 to 1500°C (note that the target sample still is at T = 900 °C). Thus, the total number of random samples generated in this example amounts to 100,000.

[99] The results of this simulation for two cases, one including electrical conductivity as a constraint and the other neglecting it, are shown in Figure 13. When the constraining parameters include the electrical conductivity, the total number of acceptable samples is 990, which represents ∼1% of the total number of generated samples. In this case, more than 90% of the samples comprising the acceptable ensemble are restricted to a temperature range of 200°C (Figure 13a), and more than 62% lies within a range of 100°C. Removing the electrical conductivity from the constraining parameters (i.e., Vp, Vs, and density only) results in an acceptable ensemble containing 2326 samples, ∼2.36% of the original samples. Approximately 90% of the ensemble now lies within a temperature range of 250°C (Figure 13b), which reflects the fact that the electrical conductivity of solid assemblages is much more sensitive to temperature changes than the other three parameters. While electrical conductivity is exponentially dependent on temperature (equation (8)) [*Jones et al.*, 2009; *Fullea et al.*, 2011], Vp, Vs, and density exhibit a quasi-linear or weakly nonlinear dependence (i.e., for most mantle phases the first temperature derivative is dominant) [see *Jones et al.*, 2009; *Afonso et al.*, 2010, and references therein].

[100] The reason for obtaining larger acceptable ensembles when temperature is included as a free parameter is twofold. First, small changes in the temperature (i.e., from one temperature bin to another) are likely to translate into small changes of the physical parameters, which in turn are likely to remain within the assigned experimental uncertainties. For instance, a change from 500 to 525°C results in changes of –2.51 kg m^{-3}, –0.008 km s^{-1}, and –0.014 km s^{-1} in density, Vs, and Vp, respectively. These variations are much smaller than the experimental uncertainties assigned to each variable (see previous section). The second factor is the well-known trade-off between temperature and composition for some parameters [e.g., seismic velocities) [*Afonso et al.*, 2010], which has the potential to convert unacceptable samples at one temperature into acceptable samples at another temperature. This is particularly evident in Figure 13b, where larger numbers of acceptable samples are found at temperatures lower than the true value. In this case, most of the samples with low FeO and low MgO, characterized by low relative densities and rejected in Figure 10, become acceptable at lower temperatures (i.e., they compensate their low compositional density with temperature). Since electrical conductivity constrains temperature better, this effect is diminished in Figure 13a (albeit still visible).

[101] If we were to adopt a frequentist point of view, it would be tempting to assign 875 and 825°C as the most likely temperatures in these ensembles. However, using the definition in item 4 in section 4.3.3 for the posterior PDF and an MCMC simulation, the most likely temperature is located within the range 875 < T < 925°C in both cases. This is depicted in Figure 13 by superimposing a color scale of the resulting marginal posterior on top of the Monte Carlo histograms. We emphasize that the histograms represent the number of samples that are compatible with data within uncertainties (frequentist analysis), while the color scale is the result of a full MCMC simulation (Bayesian analysis) with a flat prior in the temperature range 500 < T

< 1500°C. Although the marginal posterior for temperature is narrower in the case which includes electrical conductivity, the marginals for compositional parameters are slightly deteriorated in comparison to the case with Vs, Vp, and density only. This seems to be an unavoidable consequence of the intrinsic dependence of electrical conductivity on modal garnet and bulk MgO content (section 4.3.1). The addition of fluids and/or carbon-rich phases to the system would add another layer of complexity to the simultaneous treatment of Vs, Vp, density, and electrical conductivity. However, we deem that the results in this paper warrant a more comprehensive exploration of the potential benefits (temperature?) and limitations (composition?) of incorporating electrical conductivity in multiobservable inversions.

5. Conclusion

[102] In this paper, we have analyzed the main problems associated with the definitions and use of *a priori* information on compositional parameters $\rho(\mathbf{m})$ and likelihood function $L(\mathbf{m})$ for probabilistic inversion schemes aimed to constrain the thermochemical structure of the Earth's lithosphere and sublithospheric upper mantle. Within this context, the need for combining multiple geophysical datasets in a probabilistic manner has been justified and demonstrated by analyzing the sensitivity of each observable to composition and temperature, as well as their experimental uncertainties. The dependence of physical parameters such as bulk density, electrical conductivity, and seismic velocities to major-element composition has been systematically addressed using Monte Carlo simulations and an internally consistent thermodynamic formalism.

[103] Based on this analysis, we propose a general strategy to define $\rho(\mathbf{m})$ that does not rely on restrictive assumptions such as small ad hoc compositional ranges, limited/local xenolith populations, or predefined $\rho(\mathbf{m})$ for specific tectonic settings based on age-composition relationships. This is important as there is ample evidence of exceptions to such age-composition relationships; these exceptions carry significant tectonic information and are thus one of the targets to be identified by the present approach. The problem of using age-composition relationships as *a priori* information is aggravated by the fact that the likelihood, which should account for realistic uncertainties in data and theory, is only mildly sensitive to bulk compositional parameters. We have shown the intrinsic difficulties in obtaining reliable compositional estimates of peridotite samples when using geophysical parameters/observables. Most importantly, by using simple synthetic examples, we have shown that a wide range of naturally occurring compositions can equally well explain multiple geophysical data. This nonuniqueness problem is heightened at lithospheric depths, where most of the compositional variability is expected to occur, and thus, it represents a major challenge not only for traditional linearized inversions but also for explorative Monte Carlo methods. Any method attempting to estimate the compositional and thermal structure of the upper mantle should address these problems.

[104] In this first paper, we have demonstrated that a multiobservable Bayesian approach, in which the *a priori* information is based on large databases of natural mantle samples and robust correlations between major oxides offer a promising and general inference platform to address the abovementioned difficulties. The two key elements of the method are (i) the internally consistent combination of multiple geophysical observables with differential sensitivities to compositional/thermal parameters and (ii) *a priori* compositional information based on statistical analysis of large databases of natural mantle samples from many different tectonic settings. This database can be updated as more samples are analyzed, without affecting the general inversion scheme. We have shown that such approach can provide acceptable (probabilistic) estimates of both compositional variables and associated uncertainties. Nevertheless, the application of this probabilistic approach to 3-D inversion scenarios requires additional considerations at both technical and conceptual levels. We address these in detail in an accompanying paper [*Afonso et al.*, paper II, this issue].

Appendix A: Eclogites and Pyroxenites

[105] Eclogitic and pyroxenitic xenoliths are commonly recovered in both cratonic and off-craton localities around the world [*Schulze*, 1989; *Jacob*, 2004; *Griffin and O'Reilly*, 2007]. Although in most these two lithologies are subordinate in comparison to peridotite xenoliths, some localities exhibit a clear dominance of eclogites/pyroxenites in their xenolith population (e.g., Roberts Victor, South Africa). However, even in such cases, the relatively large abundance of eclogites is thought to be the result of either differential preservation effects during xenolith exhumation or sampling-depth bias [*Jacob*, 2004; *Griffin and O'Reilly*, 2007]. In fact, although their origin and role in the evolution of lithospheric mantle still are a matter of debate [*Griffin and O'Reilly*, 2007], it is commonly accepted that eclogites and pyroxenites cannot make up more than ∼1% in volume of the lithospheric mantle [*Schulze*, 1989], although higher local concentrations could exist [e.g., *Griffin and O'Reilly*, 2007; *Huang et al.*, 2012]. Since our method is designed to capture average compositional heterogeneities in the mantle with minimum vertical and horizontal extensions $\gtrsim$40 and 80 km, respectively (*Afonso et al.*, paper II, this volume), it is not suited for detecting sharp lithological contrasts or volumetrically unimportant bodies.

[106] Although beyond the scope of this paper, we note that detection of eclogitic bodies in the mantle by other geophysical techniques is also difficult task [e.g., *Ghent et al.*, 2004; *Bascou et al.*, 2001], particularly because not all eclogites are characterized by significantly different physical properties from those of peridotites. For instance, Figure A1 shows the Vs, Vp, and bulk density of 2500 randomly generated eclogitic samples based on the xenolith database of *Huang et al.* [2012]. The latter is depicted in the figure as histograms indicating the relative abundance of eclogitic xenoliths in terms of their Al_2O_3 and FeO contents. This figure also includes the Vp, Vs, and density of typical mantle peridotites at the same P-T conditions (red shaded rectangles). Except for density, which is always lower in peridotites, Vp and Vs of mantle peridotites lie within the compositional range observed in eclogitic xenoliths. More importantly, the compositional region at which the two lithologies have similar seismic velocities coincides with that of the most abundant eclogitic

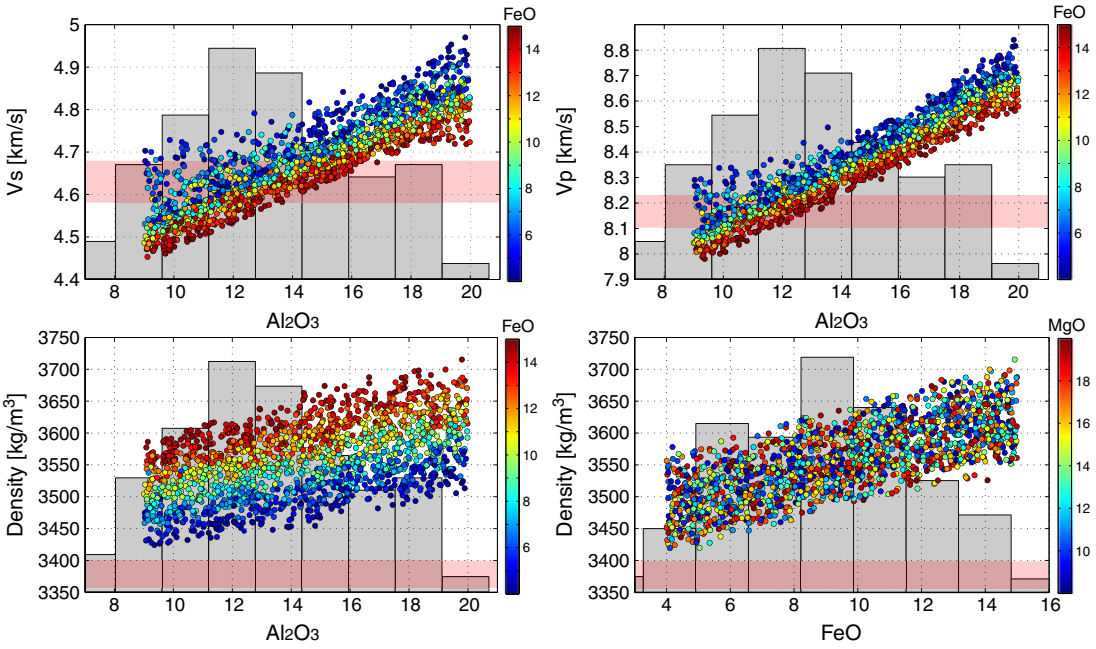

Figure A1. The figure shows the main physical parameters for 2500 random samples generated based on the database of *Huang et al.* [2012]. Color scale as in Figure 2. The histograms indicate the frequency of samples in the database. Shaded red bands denote typical values for mantle peridotite at identical P-T conditions.

xenoliths (i.e., the isotropic seismic velocities of the most commonly sampled eclogites are not too different from those of surrounding peridotites). In particular, none of the samples plotted in Figure A1 produces reflectivity coefficients >0.07, in agreement with previous studies [e.g., *Bascou et al.*, 2001; *Ji et al.*, 2003b]. This corroborates previous suggestions that the simple contrast in physical properties between peridotite and eclogite is insufficient to produce the high-amplitude reflections inferred in some localities [e.g., *Bascou et al.*, 2001; *Morgan et al.*, 2000; *Ji et al.*, 2003b]. However, interlayered heterogeneities (e.g., vertical layering of peridotite-eclogite) with the proper thickness could produce local constructive interference and high reflectivity.

Appendix B: Na-CFMAS and H2O-CFMAS Versus CFMAS

[107] The addition of Na2O to the CFMAS system requires additional end members and more elaborated solid-solution models than in the simpler CFMAS system. This translates into much longer computation times in the energy minimization problem, and thus, the performance of the inversion scheme is deteriorated. Therefore, the following question arises: does the inclusion of Na2O into the CFMAS system improve the result of the inversion scheme to a significant extent? In order to answer this question, we have run a number of Monte Carlo simulations at different P-T conditions and for different compositions. Figure B1 shows the results of one of such simulations for identical P-T-C conditions as those used to obtain Figure 11. A visual comparison of these figures suggest that the recovered fields of high a posteriori probability (solution to the inverse problem) with and without Na2O are almost identical. Similar results were obtained for other peridotite compositions and P-T conditions. Based on these results, and considering the modest sensitivity of geophysical observables to bulk composition, we conclude that there is no practical justification for, or obvious advantage in, including Na2O in our inversion. We note, however, that this is strictly valid if the assumption of an upper mantle dominated by peridotite holds true. If large amounts of basaltic or eclogitic material (>20 vol% of "normal" mantle) are present as mechanically and chemically independent lithologies, the need to consider Na2O in the computation could be justified [e.g., *Xu et al.*, 2008]. More work towards subjecting the "mixture hypothesis" to a rigorous probabilistic test (using geophysical observables) and geochemical/petrological arguments will be needed.

[108] The addition of water to the system implies a substantial increase in the number of phases (e.g., micas and amphiboles) and solution models that need to be considered during the minimization problem. The computation time necessary to solve one minimization problem within the H2O-CFMAS can be as large as fivefold or more compared to the dry counterpart. We have explored the effects of including H2O in our computations by using a modified-augmented version of *Holland and Powell*'s [1998] thermodynamic database as described in *Connolly and Kerrick* [2002] and *Afonso and Zlotnik* [2011]. We found that, as an approximate rule-of-thumb, for every 1 wt% increase in H2O, there is a decrease of 1% and 2% in the anharmonic Vs and bulk density of peridotites, respectively, due to the appearance of "soft" hydrous minerals. This is consistent with other previous estimations [e.g., *Carlson and*

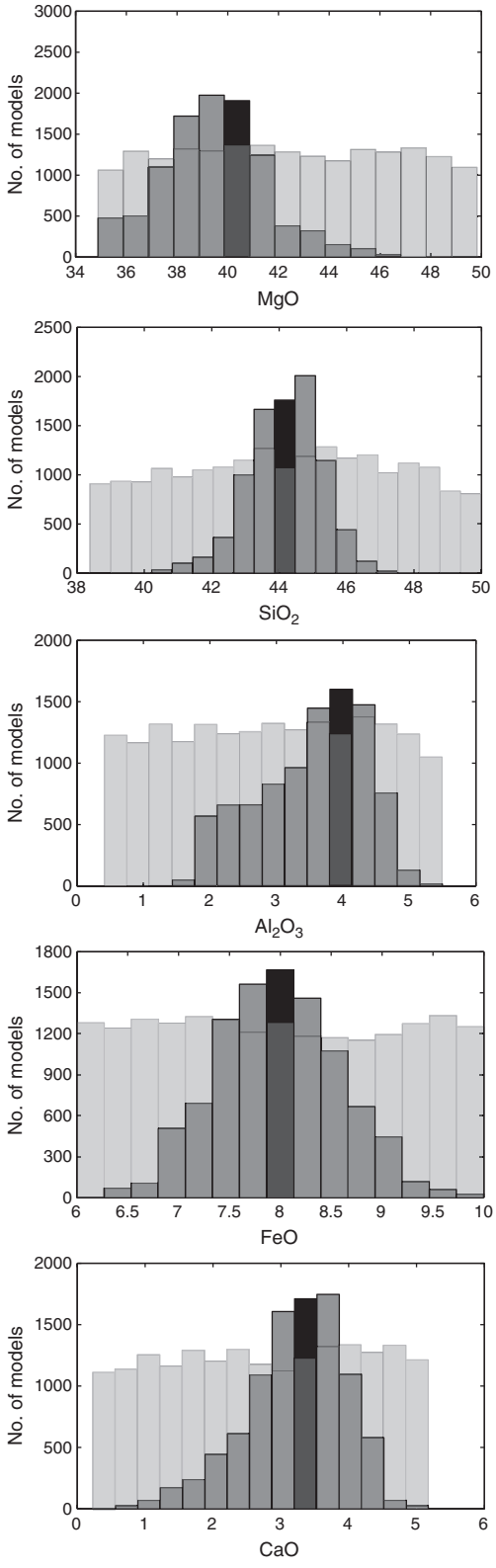

Figure B1. Results from an MCMC simulation using the same target composition and P-T conditions as in Figure 11, but including Na2O in the energy minimization problem. The thermodynamic database and formalism are those of *Stixrude and Lithgow-Bertelloni* [2011].

Miller, 2003]. Since the typical water content in SCLM rocks is <400 ppm, or ∼0.04 wt%, the expected anharmonic Vs and density reductions are ∼0.04% and 0.08%, respectively. Even in localized areas of volatile-rich peridotites (e.g., metasomatized veins/conduits) with average water contents twice or three times as high, the associated decrease in Vs and density is not expected reach 0.1% and 0.2%, respectively. Therefore, variations in water content of the order of a few hundreds ppm can be ignored when dealing with seismic and/or gravity data (except, of course, in subduction zone environments). Electrical conductivity, on the other hand, is much more sensitive to small variations in water content in mantle rocks, and in principle, it could be used to infer water contents that other observables cannot detect [*Jones et al.*, 2012]. The difficulty is that the necessary experimental information on the effects that water has on the conductivity of mantle minerals at upper mantle conditions still is subject to debate [see discussion in *Jones et al.*, 2012]. Also, water-assisted attenuation effects on nominally anhydrous phases [*Karato*, 2012, and references therein] has not been included in this study due to the lack of robust quantitative models. However, due to the low water content in SCLM rocks, this effect also would be negligible. Although a thorough exploration of the possibility of mapping "water anomalies" is beyond the scope of this paper, we note that our method is perfectly suitable to accommodate such possibility.

Appendix C: Gravity and Geoid Sensitivities to Shallow/Deep Density Structures

[109] Geoid anomalies are more sensitive to deep density variations than gravity anomalies, and therefore, they represent an important constraint in lithospheric modeling. Figure C1 shows a synthetic model with two topographic heights, one is compensated purely by crustal isostasy and the other purely by thermal (lithospheric) isostasy. The difference between these two heights in terms of the Bouguer anomaly is only <18 mGals. Such low values could easily be masked by small density variations at shallow levels and therefore, it would be difficult to identify the thinning in the lithosphere. The geoid anomaly, on the other hand, exhibits a difference of >8 m. This value would be difficult to explain by shallow density anomalies only, particularly because the magnitude of the anomalies required to explain the geoid would seriously perturb the predicted topography.

Appendix D: Different Compositions and PT Conditions

[110] The Bayesian strategy described in the text has been justified by the results it predicts, but results for only one composition at specific P-T conditions were shown. Here, we show the method still is able to retrieve a robust estimate of the true composition when the target composition or the P-T conditions are changed.

[111] Figure D1 shows the results from an MCMC simulation using the steps described in the text for a different, more depleted, composition (SiO_2 = 44.04, Al_2O_3 = 1.26, FeO = 6.52, MgO = 46.95, and CaO = 1.21). Note that the

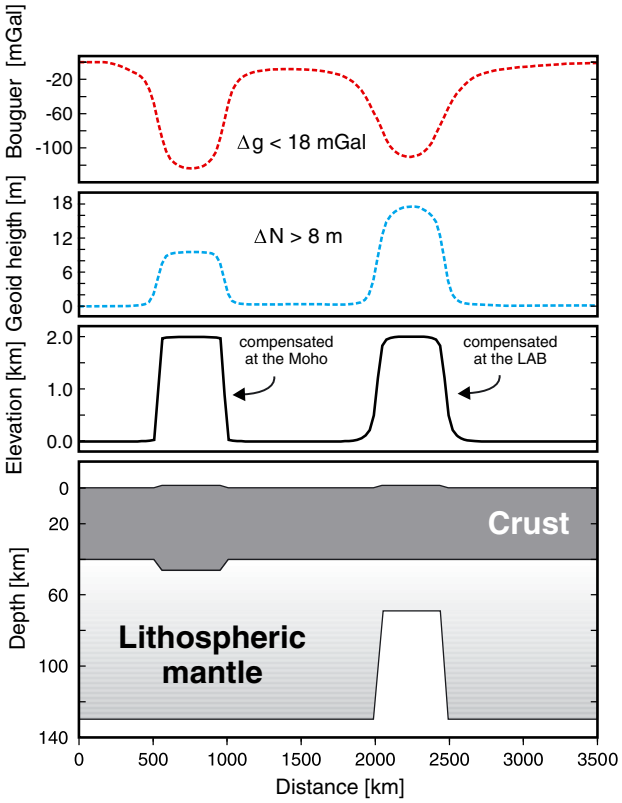

Figure C1. Bouguer and geoid anomalies associated with two topographic heights. Both heights have the same absolute elevation, but their isostatic compensation is achieved at different depths. The bottom of the lithosphere (LAB) is defined as the 1315°C isotherm. Note the large difference in geoid height between the two topographic heights. Computations are performed with LitMod2D [*Afonso et al.*, 2008].

prior histograms have been narrowed towards the true value in the posterior. In this case, however, FeO is not particularly well constrained. This is due to the fact that for this particular bulk composition, the trend defined by samples that fit the data equally well (such as the one in Figure 10) lies well within the region defined by our compositional prior. Since the likelihood function is only mildly sensitive to compositional parameters (section 4.3.1), it cannot overwhelm the vague prior and produce a peak around the true value. Nevertheless, the region of high posterior probability successfully encloses the true value.

[112] Figure D2 shows the results from a regular Monte Carlo search of acceptable samples (as in Figure 10) for two different T-P conditions. While the composition is identical in the two runs, the ensembles in Figures D2a–D2d have been obtained at T = 900 °C and P = 3 GPa and those in Figures D2e–D2h at T = 1447 °C and P = 11 GPa. As explained in the text, the combined effects of larger rations gt/opx and the decrease in the capacity of pyroxenes to accommodate Al_2O_3 as pressure increases results in a greater sensitivity of Vp, Vs, and bulk density to changes in composition. This is reflected in the reduction of the high-Mg/low-Al/high-Fe to low-Mg/high-Al/low-Fe trend in the ensemble of acceptable samples shown in Figures 10 and

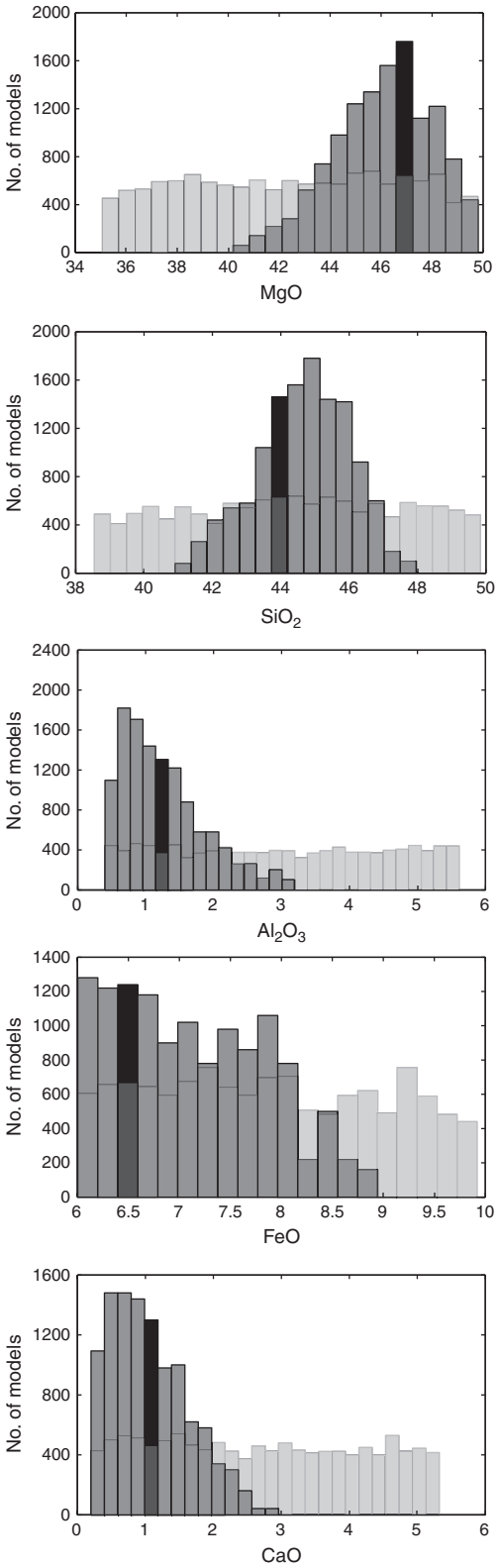

Figure D1. Prior (transparent) and posterior (dark gray) histograms from an MCMC simulation performed following the steps explained in the text. The P-T conditions are identical to those in Figure 11, but with a different compositions (SiO_2 = 44.04, Al_2O_3 = 1.26, FeO = 6.52, MgO = 46.95, and CaO = 1.21). The bin containing the true value is colored black.

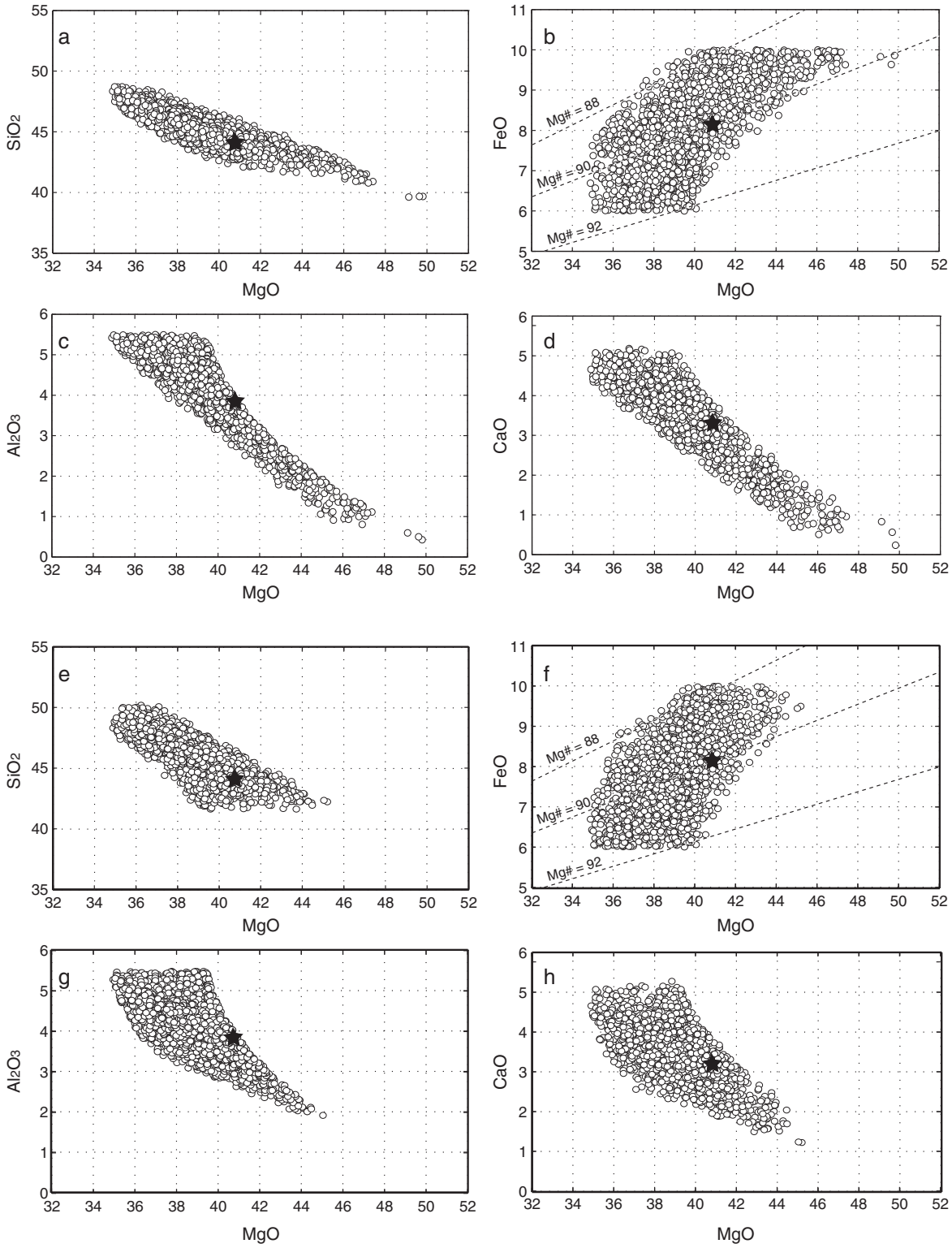

Figure D2. Ensemble of acceptable samples from a Monte Carlo search with 5500 random samples at two different P-T conditions [(a–d) T = 900 °C and P = 3 GPa; (e–h): T = 1447 °C and P = 11 GPa]. Note that the high-Mg/low-Al/high-Fe to low-Mg/high-Al/low-Fe trend at P-T conditions pertaining to the lithospheric mantle (Figures D2a–D2d; also Figure 10) is reduced at high P-T conditions (Figures D2e–D2h). The sensitivity of parameters Vs, Vp, and density to compositional parameters tends to increase with pressure. The true compositions is indicated by the black star. Only anharmonic velocities are used.

D2a–D2d (high-pressure ensembles tends to form a more cluster-like shape).

[113] **Acknowledgments.** We thank M. Fernàndez and A. Khan for their critical reading of a preliminary version of this manuscript. Also, we thank S. Fishwick, Uli Faul, and an anonymous reviewer for their insightful and constructive reviews. Discussions with M. Sambridge, N. Rawlinson, B. Kennett, S. Lebedev, and the participants of the workshop ThermoDynaMix III are acknowledged. The works of JCA and YY have been supported by an Australian Research Council Discovery grant (DP120102372). AGJ acknowledges financial support from Science Foundation Ireland (grants 07/RFP/GEOF759 and 10/IN.1/I3022-STTF 11). JF was supported by an SFI PI grant (10/IN.1/I3022) to AGJ for IRETHERM (http://www.iretherm.ie), by the JAE-DOC programme (CSIC-Spain), and by Spanish Ministry of Economy and Competitiveness grant CGL2012-37222. This is contribution 217 from the Australian Research Council Centre of Excellence for Core to Crust Fluid Systems (http://www.ccfs.mq.edu.au) and 855 in the GEMOC Key Centre (http://www.gemoc.mq.edu.au).

References

Afonso, J. C., G. Ranalli, and M. Fernàndez (2005), Thermal expansivity and elastic properties of the lithospheric mantle: Results from mineral physics of composites, *Phys. Earth Planet. Int.*, *149*, 279–306, doi:10.1016/j.pepi.2004.10.003.

Afonso, J. C., M. Fernàndez, G. Ranalli, W. L. Griffin, and J. A. D. Connolly (2008), Integrated geophysical-petrological modelling of the lithospheric-sublithospheric upper mantle: Methodology and applications, *Geochem. Geophys. Geosyst.*, *9*, Q05008, doi:10.1029/2007GC001834.

Afonso, J. C., and S. Zlotnik (2011), The subductability of the continental lithosphere: The before and after story, in *Arc-Continent Collision*, edited by D. Brown, and P. D. Ryan, Springer, New York, 5386, doi: 10.1007/978-3-540-88558.

Afonso, J. C., and D. Schutt (2012), The effects of polybaric partial melting on the density and seismic velocities of mantle restites, *Lithos*, *134-135*, 289–303, doi:10.1016/j.lithos.2012.01.009.

Afonso, J. C., G. Ranalli, M. Fernàndez, W. L. Griffin, S. Y. O'Reilly, and U. Faul (2010), On the Vp/Vs - Mg# correlation in mantle peridotites: Implications for the identification of thermal and compositional anomalies in the upper mantle, *Earth Planet. Sci. Lett.*, *289*, 606–618, doi:10.1016/j.epsl.2009.12.005.

Ahrens, T. J. (ed.) (1995), *Mineral Physics & Crystallography: A Handbook of Physical Constants*, 354, AGU Ref. Shelf, vol. 2, AGU, Washington, D. C., doi:10.1029/RF002.

Amaru, M. L., W. Spakman, A. A. Villaseñor, S. Sandoval, and E. Kissling (2008), A new absolute arrival time data set for Europe, *Geophys. J. Int.*, *173*, 465–472, doi:10.1111/j.1365-246X.2008.03704.x.

Anderson, O. L. (1995), *Equations of State of Solids for Geophysics and Ceramic Science*, Oxford University Press, Oxford.

Bailey, I. W., M. S. Miller, K. Liu, and A. Levander (2012), VS and density structure beneath the Colorado Plateau constrained by gravity anomalies and joint inversions of receiver function and phase velocity data, *J. Geophys. Res.*, *117*, B02313, doi:10.1029/2011JB008522.

Bailey, R. C. (1970), Inversion of the geomagnetic induction problem, *Proc. R. Soc. London*, *A315*, 185–194.

Bascou, J., G. Barruol, A. Vauchez, D. Mainprice, and M. Egydio-Silva (2001), EBSD-measured lattice-preferred orientations and seismic properties of eclogites, *Tectonophysics*, *342*(1-2), 61–80.

Bass, J. D., and D. L. Anderson (1984), Composition of the upper mantle: Geophysical tests of two petrological models, *Geophys. Res. Lett.*, *11*(3), 229–232, doi:10.1029/GL011i003p00229.

Becker, J. J., et al. (2009), Global bathymetry and elevation data at 30 arc seconds resolution: SRTM30_PLUS, *Mar. Geod.*, *32*, 355–371.

Becker, T. W. (2012), On recent seismic tomography for the western United States, *Geochem. Geophys. Geosyst.*, *13*, Q01W10, doi:10.1029/2011GC003977.

Berryman, J. G. (1995), Mixture theories for rock properties, in *Rock Physics & Phase Relations: A Handbook of Physical Constants*, edited by T. J. Ahrens, AGU Ref. Shelf, vol. 3, AGU, Washington, D. C., 205–228, doi:10.1029/RF003p0205.

Biegler, L. et al. (eds.) (2011), *Large-Scale Inverse Problems and Quantification of Uncertainty*, Wiley and Sons, UK.

Birch, F. (1961), The velocity of compressional waves in rocks to 10 kbar, Part 2, *J. Geophys. Res.*, *66*, 2199–2224.

Bodinier, J.-L., C. J. Garrido, I. Chanefo, O. Bruguier, and F. Gervilla (2008), Origin of pyroxenite-peridotite veined mantle by refertilization reactions: Evidence from the ronda peridotite (Southern Spain), *J. Petrology*, *49*(5), 999–1025, doi:10.1093/petrology/egn014.

Bosch, M. (1999), Lithologic tomography: From plural geophysical data to lithology estimation, *J. Geophys. Res.*, *104* (B1), 749–766, doi:10.1029/1998JB900014.

Brooks, S., A. Gelman, G. L. Jones, and X.-L. Meng (eds.) (2011), *Handbook of Markov Chain Monte Carlo*, Chapman and Hall/CRC, USA.

Brown, M., and T. Rushmer (eds.) (2006), *Evolution and Differentiation of the Continental Crust*, Cambridge University Press, Cambridge.

Butcher, J. B., Medina, M. A., Jr., and C. M. Marin (1991), Empirical Bayes regionalization methods for spatial stochastic processes, *Water Resour. Res.*, *27*(1), 7–15, doi:10.1029/90WR01879.

Cammarano, F., P. Tackley, and L. Boschi (2011), Seismic, petrological and geodynamical constraints on thermal and compositional structure of the upper mantle: Global thermo-chemical models, *Geophys. J. Int.*, *187*, 1301–1318, doi:10.1111/j.1365-246X.2011.05223.X.

Carlin, B. P., and T. A. Louis (2000), *Bayes and Empirical Bayes Methods for Data Analysis* 2nd ed., Chapman and Hall/CRC, USA.

Chappell, A. R., and N. J. Kusznir (2008), Three-dimensional gravity inversion for Moho depth at rifted continental margins incorporating a lithosphere thermal gravity anomaly correction, *Geophys. J. Int.*, *174*(1), 1–13, doi:10.1111/j.1365-246X.2008.03803.X.

Chave, A. D. (2012), Estimation of the magnetotelluric response function, in *The Magnetotelluric Method: Theory and Practice*, edited by A. D. Chave, and A. G. Jones, Chapter 5, Cambridge University Press, Cambridge (UK) .

Chave, A. D., and A. G. Jones (1997), Electric and magnetic field galvanic distortion decomposition of BC87 data, *J. Geomag. Geoelec.*, *49*(6), 767–789.

Christensen, N. I., and W. D. Mooney (1995), Seismic velocity structure and composition of the continental crust: A global view, *J. Geophys. Res.*, *100*, 9761–9788.

Carlson, R. L., and D. J. Miller (2003), Mantle wedge water contents estimated from seismic velocities in partially serpentinized peridotites, *Geophys. Res. Lett.*, *30*, 1250, doi:10.1029/2002GL016600.

Clauser, C., and E. Huenges (1995), Thermal conductivity of rocks and minerals, in *Rock Physics and Phase Relations: A Handbook of Physical Constants*, edited by T. J. Ahrens, AGU Reference Shelf, vol. 3, 105–126.

Connolly, J. A. D. (2009), The geodynamic equation of state: What and how, *Geochem. Geophys. Geosys.*, *10*, Q10014, doi:10.1029/2009GC002540.

Connolly, J. A. D., and D. M. Kerrick (2002), Metamorphic controls on seismic velocity of subducted oceanic crust at 100-250 km depth, *Earth Planet. Sci. Lett.*, *204*, 61–74.

Crameri, F., H. Schmeling, G. J. Golabek, T. Duretz, R. Orendt, S. J. H. Buiter, D. A. May, B. J. P. Kaus, T. V. Gerya, and P. J. Tackley (2012), A comparison of numerical surface topography calculations in geodynamic modelling: An evaluation of the 'sticky air' method, *Geophys J. Int.*, *189*, 38–54, doi:10.1111/j.1365-246X.2012.05388.X.

Dalton, C. A., and U. H. Faul (2010), The oceanic and cratonic upper mantle: Clues from joint interpretation of global velocity and attenuation models, *Lithos*, *120*, 160–172, doi:10.1016/j.lithos.2010.08.020.

Davies, J., and D. Davies (2010), Earth's surface heat flux, *Solid Earth*, *1*, 5–24, doi:10.5194/se-1-5-2010.

de Wit, R. W. L., J. Trampert, and R. D. van der Hilst (2012), Toward quantifying uncertainty in travel time tomography using the null-space shuttle, *J. Geophys. Res.*, *117*, B03301, doi:10.1029/2011JB008754.

Deen, T., W. L. Griffin, G. Begg, S. Y. O'Reilly, and L. M. Natapov (2006), Thermal and compositional structure of the subcontinental lithospheric mantle: Derivation from shear-wave seismic tomography, *Geochem. Geophys. Geosys.*, *7*, Q07003, doi:10.1029/2005GC001120.

Diment, W. H., and H. R. Pratt, (1988), Thermal conductivity of some rock-forming minerals: A tabulation, *Open file report 88-690*, U.S. Geol. Survey.

Duijndam, A. J. W. (1988), Bayesian estimation in seismic inversion. Part I: Principles, *Geophys. Prospect.*, *36*, 878–898.

Ebbing, J., C. Braitenberg, and H.-J. Gøtze (2006), The lithospheric density structure of the Eastern Alps, *Tectonophysics*, *414*, 145–155, doi:10.1016/j.tecto.2005.10.015.

Efron, B. (2010), *Large-Scale Inference: Empirical Bayes Methods for Estimation, Testing, and Prediction*, Cambridge University Press, Cambridge.

El-Hinnawi, E. E. (1966), *Methods in Chemical and Mineral Microscopy*, 222, Elsevier, Amsterdam.

Eisel, M., and G. D. Egbert (2001), On the stability of magnetotelluric transfer function estimates and the reliability of their variances, *Geophys. J. Int.*, *144*(1), 65–82.

Fernàndez, M., J. C. Afonso, and G. Ranalli (2010), The deep lithospheric structure of the Namibian volcanic margin, *Tectonophysics*, *481*, 68–81, doi:10.1016/j.tecto.2009.02.036.

Fishwick, S. (2010), Surface wave tomography: Imaging of the lithosphere-asthenosphere boundary beneath central and southern Africa? *Lithos*, *120*, 63–73, doi:10.1016/j.lithos.2010.05.011.

Fullea, J., J. C. Afonso, J. A. D. Connolly, M. Fernàndez, D. Garcia-Castellanos, and H. Zeyen (2009), LitMod3D: An interactive 3-D software to model the thermal, compositional, density, seismological, and rheological structure of the lithosphere and sublithosheric upper mantle, *Geochem. Geophys. Geosyst.*, *10*, Q08019, doi:10.1029/2009GC002391.

Fullea, J., M. Fernàndez, J. C. Afonso, J. Vergés, and H. Zeyen (2010), The structure and evolution of the lithosphere-asthenosphere boundary beneath the Atlanitc-Mediterranean Transition Region, *Lithos*, *120*, 74–95.

Fullea, J., M. R. Muller, and A. G. Jones (2011), Electrical conductivity of continental lithospheric mantle from integrated geophysical and petrological modeling: Application to the Kaapvaal Craton and Rehoboth Terrane, southern Africa, *J. Geophys. Res.*, *116*, B10202, doi:10.1029/2011JB008544.

Ghent, E. D., G. M. Dipple, and J. K. Russell (2004), Thermodynamic models for eclogitic mantle lithosphere, *Earth Planet. Sci. Lett.*, *218*, 451–462, doi:10.1016/S0012-821X(03)00678-2.

Gilks, W. R., S. Richardson, and D. J. Spiegelhalter (eds.) (1996), *Markov Chain Monte Carlo in Practice*, Chapman and Hall, USA.

Gouveia, W. P., and J. A. Scales (1998), Bayesian seismic waveform inversion: Parameter estimation and uncertainty analysis, *J. Geophys. Res.*, *103*(B2), 2759–2779, doi:10.1029/97JB02933.

Griffin, W. L., S. O'Reilly, J. C. Afonso, and G. Begg (2009), The composition and evolution of lithospheric mantle: A re-evaluation and its tectonic implications, *J. Petrol.*, *50*(7), 1185–1204, doi:10.1093/petrology/egn033.

Griffin, W. L., S. Y. O'Reilly, and C. G. Ryan (1999), The composition and origin of sub-continental lithospheric mantle, in *Mantle Petrology: Field Observations and High-Pressure Experimentation: A Tribute to Francis R. (Joe) Boyd*, edited by Y. Fei, C. M. Berkta, and B. O. Mysen, The Geochemical Society, Special Publication No 6., Houston, Tex., 13–45.

Griffin, W. L., and S. Y. O'Reilly (2007), Cratonic lithospheric mantle: Is anything subducted?, *Episodes*, *30*(1), 43–53.

Griffin, W. L., S. Y. Wass, and J. D. Hollis (1984), Ultramafic xenoliths from Bullenmerri and Gnotuk maars, Victoria, Australia: Petrology of a subcontinental crust-mantle transition, *J. Petrology*, *25*, 53–87.

Griffin, W. L., A. Zhang, S. Y. O'Reilly, and C. G. Ryan (1998), Phanerozoic evolution of the lithosphere beneath the Sino-Korean Craton, in *Mantle Dynamics and Plate Interactions in East Asia*, edited by M. Flower, S. L. Chung, C. H. Lo, and T. Y. Lee, vol. 27, *Amer. Geophys. Union Geodynamics*, AGU, Washington, D. C., 107–126.

Groom, R. W., and R. C. Bailey (1989), Decomposition of magnetotelluric impedance tensors in the presence of local three dimensional galvanic distortion, *J. Geophys. Res.*, *94*, 1913–1925.

Gudmundsson, O., J. H. Davies, and R. W. Clayton (1990), Stochastic analysis of global traveltime data: Mantle heterogeneity and random errors in the ISC data, *Geophys. J. Int.*, *102*, 24–43.

Hasterok, D., and D. S. Chapman (2007), Continental thermal isostasy: 1. Methods and sensitivity, *J. Geophys. Res.*, *112*, B06414, doi:10.1029/2006JB004663.

Herzberg, C. (2004), Geodynamic information in peridotite petrology, *J. Petrol.*, *45*, 2507–2530, doi:10.1093/petrology/egh039.

Herzberg, C., and M. J. O'Hara (2002), Plume-associated ultramafic magmas of Phanerozoic age, *J. Petrol.*, *43*, 1857–1883.

Hieronymus, C. F., and S. Goes (2010), Complex cratonic seismic structure from thermal models of the lithosphere: Effects of variations in deep radiogenic heating, *Geophys. J. Int.*, *180*, 999–1012, doi:10.1111/j.1365-246X.2009.04478.X.

Hirose, K., and T. Kawamoto (1995), Hydrous partial melting of lherzolite at 1 GPa: The effect of H2O on the genesis of basaltic magmas, *Earth Planet. Sci. Lett.*, *133*, 463–473.

Hirschmann, M. M. (2006), Water, melting, and the deep Earth's H2O cycle, *Ann. Rev. Earth Planet. Sci.*, *34*, 629–653, doi:10.1146/annurev.earth.34.031405.125211.

Hofmann, A. W. (1997), Mantle geochemistry: The message from oceanic volcanism, *Nature*, *385*, 219–229, doi:10.1038/385219a0.

Holland, T., and R. Powell (1998), An internally consistent thermodynamic data set for phases of petrological interest, *J. Metamorph. Geol.*, *16*, 309–343.

Huang, J.-X., Y. Greau, W. L. Griffin, S. Y. O'Reilly, and N. Pearson (2012), Multi-stage origin for Roberts Victor eclogites: Isotopic evidence for metasomatic processes, *Lithos*, *142-143*, 161–181, doi:10.1016/j.lithos.2012.03.002.

Idier, J. (2008), *Bayesian Approach to Inverse Problems*, Wiley and Sons, UK.

Irifune, T., and A. E. Ringwood (1993), Phase transformations in subducted oceanic crust and buoyancy relationships at depths of 600-800 km in the mantle, *Earth Planet. Sci. Lett.*, *117*, 101–110.

Jacob, D. E. (2004), Nature and origin of eclogite xenoliths, *Lithos*, *77*, 295–316, doi:10.1016/j.lithos.2004.03.038.

Jacoby, W., and P. L. Smilde (2009), *Gravity Interpretation*, Springer, Berlin.

Jackson, I., J. D. FitzGerald, U. H. Faul, and B. H. Tan (2002), Grain-size-sensitive seismic wave attenuation in polycrystaline olivine, *J. Geophys. Res.*, *107*, B122360.

Jackson, I., and U. H. Faul (2010), Grainsize-sensitive viscoelastic relaxation in olivine: Towards a robust laboratory-based model for seismological application, *Phys. Earth Planet. Int.*, *183*, 151–163, doi:10.1016/j.pepi.2010.09.005.

James, D. E., F. R. Boyd, D. Schutt, D. R. Bell, and R. W. Carlson (2004), Xenolith constraints on seismic velocities in the upper mantle beneath southern Africa, *Geochem. Geophys. Geosys.*, *5*, Q01002, doi:10.1029/2003GC000551.

Jaupart, C., and J.-C. Mareschal (2011), *Heat Generation and Transport in the Earth*, Cambridge University Press, Cambridge.

Ji, S., K. Saruwatari, D. Mainprice, R. Wirth, Z. Xu, and B. Xia (2003b), Microstructures, petrofabrics and seismic properties of ultra high-pressure eclogites from Sulu region, China: Implications for rheology of subducted continental crust and origin of mantle reflections, *Tectonophysics*, *370* (1-4), 49–76, doi:10.1016/S0040-1951(03)00177-X.

Ji, S. (2004), A generalized mixture rule for estimating the viscosity of solid-liquid suspensions and mechanical properties of polyphase rocks and composite materials, *J. Geophys. Res.*, *109*, B10207, doi:10.1029/2004JB003124.

Ji, S., P. Zhao, and B. Xia (2003a), Flow laws of multiphase materials and rocks from end-member flow laws, *Tectonophysics*, *370*, 129–145, doi:10.1016/S0040-1951(03)00182-3.

Jiménez-Munt, I., M. Fernàndez, J. Vergés, and J. P. Platt (2008), Lithosphere structure underneath the Tibetan Plateau inferred from elevation, gravity and geoid anomalies, *Earth. Planet. Sci. Lett.*, *267*, 276–289, doi:10.1016/j.epsl.2007.11.045.

Jokinen, J., and I. T. Kukkonen (1999), Random modelling of the lithospheric thermal regime: Forward simulations applied in uncertainty analysis, *Tectonophysics*, *306*, 277–292.

Jones, A. G. (1988), Static shift of magnetotelluric data and its removal in a sedimentary basin environment, *Geophysics*, *53*(7), 967–978.

Jones, A. G. (1999), Imaging the continental upper mantle using electromagnetic methods, *Lithos*, *48*(1-4), 57–80.

Jones, A. G. (2012), Distortion of magnetotelluric data: its identification and removal, in *The Magnetotelluric Method: Theory and Practice*, edited by Chave, A. D., and A. G. Jones, Chapter 6, Cambridge University Press, Cambridge (UK).

Jones, A. G., and I. J. Ferguson (2001), The electric moho, *Nature*, *409* (6818), 331–333.

Jones, A. G., R. L. Evans, and D. W. Eaton (2009), Velocity-conductivity relationships for mantle mineral assem1 blages in Archean cratonic lithosphere based on a review of laboratory data and HashinShtrikman extremal bounds, *Lithos*, *109*, 131–143, doi:10.1016/j.lithos.2008.10.014.

Jones, A. G., J. Fullea, R. L. Evans, and M. R. Muller (2012), Water in cratonic lithosphere: Calibrating laboratory-determined models of electrical conductivity of mantle minerals using geophysical and petrological observations, *Geochem. Geophys. Geosyst.,* in press., doi:10.1029/2012GC004055, in press.

Kaban, M. K., M. Tesauro, and C. Cloetingh (2010), An integrated gravity model for Europe's crust and upper mantle, *Earth Planet. Sci. Lett.*, *296*(3-4), 195–209, doi:10.1016/j.epsl.2010.04.041.

Kaban, M. K., P. Schwintzer, and S. A. Tikhotsky (1999), A global isostatic gravity model of the earth, *Geophys. J. Int.*, *136*, 519–536.

Karato, S.-I. (2008), *Deformation of Earth Materials*, Cambridge University Press, Cambridge.

Karato, S.-I. (2012), On the origin of the asthenosphere, *Earth Planet. Sci. Lett.*, *321-322*, 95–103, doi:10.1016/j.epsl.2012.01.001.

Kelemen, P. B, S. T. Hart, and S. Bernstein (1998), Silica enrichment in the continental upper mantle via melt/rock reaction, *Earth Planet. Sci. Lett.*, *164*, 387–406.

Khan, A., A. Zunino, and F. Deschamps (2011b), The thermo-chemical and physical structure beneath the North American continent from Bayesian inversion of surface-wave phase velocities, *J. Geophys. Res.*, *116*, B09304, doi:10.1029/2011JB008380.

Khan, A., J. A. D. Connolly, and N. Olsen (2006), Constraining the composition and thermal state of the mantle beneath Europe from inversion

of long-period electromagnetic sounding data, *J. Geophys. Res.*, *111*, B10102, doi:10.1029/2006JB004270.

Khan, A., J. A. D. Connolly, J. Maclennan, and K. Mosegaard (2007), Joint inversion of seismic and gravity data for lunar composition and thermal state, *Geophys. J. Int.*, *168*, 243, doi:10.1111/j.1365-246X.2006.03200.X.

Khan, A., L. Boschi, and J. A. D. Connolly (2011a), Mapping the Earth's thermochemical and anisotropic structure using global surface wave data, *J. Geophys. Res.*, *116*, B01301, doi:10.1029/2010JB007828.

Kitanidis, P. K. (2011a), Bayesian and geostatistical approaches to inverse problems, in *Large-Scale Inverse Problems and Quantification of Uncertainty*, edited by L. Biegler et al., Wiley and Sons, UK.

Kitanidis, P. K. (2011b), Generalized priors in Bayesian inversion problems, *Adv. Water Res.*, *36*, 3–10, doi:10.1016/j.advwatres.2011.05.005.

Korenaga, J., W. S. Holbrook, R. S. Detrick, and P. B. Kelemen (2001), Gravity anomalies and crustal structure across the Southeast Greenland margin, *J. Geophys. Res.*, *106*, 8853–8870.

Kukkonen, I. T., and P. Peltonen (1999), Xenolith-controlled geotherm for the central Fennoscandian Shield: Implications for lithosphere-asthenosphere relations, *Tectonophysics*, *304*, 301–315.

Kuskov, O. L., V. A. Kronrod, and A. A. Prokofev (2011), Thermal structure and thickness of the lithospheric mantle underlying the Siberian Craton from the Kraton and Kimberlit superlong seismic profiles, *Izv. Phys. Solid Earth*, *47*, 155–175, doi:10.1134/S1069351310111011.

Lachenbruch, A. H., and P. Morgan (1990), Continental extension, magmatism, and elevation: Formal relations and rules of thumb, *Tectonophysics*, *174*, 39–62.

Ledo, J., A. G. Jones, I. J. Ferguson, and L. Wolynec (2004), Lithospheric structure of the Yukon, northern Canadian Cordillera, obtained from magnetotelluric data, *J. Geophys. Res.*, *109* (B4), doi:10.1029/2003JB002516.

Lee, C.-T. A. (2003), Compositional variation of density and seismic velocities in natural peridotites at stp conditions: Implications for seismic imaging of compositional heterogeneites in the upper mantle, *J. Geophys. Res.*, *108*, doi:10.1029/2003JB002,413.

Li, C., R. D. van der Hilst, A. S. Meltzerb, and E. R. Engdahl (2008), Subduction of the Indian lithosphere beneath the Tibetan Plateau and Burma, *Earth Planet. Sci. Lett.*, *274*, 157–168, doi:10.1016/j.epsl.2008.07.016.

Lin, F.-C., M. H. Ritzwoller, and R. Snieder (2009), Eikonal Tomography: Surface wave tomography by phase-front tracking across a regional broad-band seismic array, *Geophys. J. Int.*, *177*(3), 1091–1110, doi:10.1111/j.1365-246X.2009.04105.x.

Lithgow-Bertelloni, C., and P. G. Silver (1998), Dynamic topography, plate driving forces and the African superswell, *Nature*, *395*, 269–272.

Malinverno, A., and V. A. Briggs (2004), Expanded uncertainty quantification in inverse problems: Hierarchical Bayes and empirical Bayes, *Geophysics*, *69*, 1005–1016, doi:10.1190/1.1778243.

Marquart, G., and H. Schmeling (1989), Topography and geoid undulations caused by small scale convection beneath continental lithosphere of variable elastic thickness, *Geophys. J. Int.*, *97*, 511–527, doi:10.1111/j.1365-246X.1989.tb00520.X.

Matsukage, K. M., Y. Nishihara, and S. I. Karato (2005), Seismological signature of chemical differentiation of Earth's upper mantle, *J. Geophys. Res.*, *110*, B12305, doi:10.1029/2004JB003.

McNeice, G. W., and A. G. Jones (2001), Multisite, multifrequency tensor decomposition of magnetotelluric data, *Geophysics*, *66*(1), 158–173.

Meissner, R. (1986), *The Continental Crust: A Geophysical Approach*, Int. Geophys. Series, vol. 34, Academic Press, London.

Mooney, W. D., and J. E. Vidale (2003), Thermal and chemical variations in subcrustal cratonic lithosphere: Evidence from crustal isostasy, *Lithos*, *71*, 185–193, doi:10.1016/j.lithos.2003.07.004.

Morgan, R. P. L, P. J. Barton, M. Warner, J. Morgan, C. Price, and K. Jones (2000), Lithospheric structure north of Scotland-I P-wave modelling, deep reflection profiles and gravity, *Geophys. J. Int.*, *142*, 716–736.

Mosegaard, K. (1998), Resolution analysis of general inverse problems through inverse Monte Carlo sampling, *Inverse Prob.*, *14*, 405–426.

Mosegaard, K., and A. Tarantola (2002), *Probabilistic Approach to Inverse Problems: Chapter for the International Handbook of Earthquake and Engineering Seismology*, 237–265, Academic Press, New York.

Mosegaard, K., and M. Sambridge (2002), Monte Carlo analysis of inverse problems, *Inverse Prob.*, *18*, R29–R54.

Nakiboglu, S. M., and K. Lambeck (1985), Comments on thermal isostasy, *J. Geodyn.*, *2*, 51–65.

Naus-Thijssen, F. M. J., A. J. Goupee, S. S. Vel, and S. E. Johnson (2011), The influence of microstructure on seismic wave speed anisotropy in the crust: Computational analysis of quartz-muscovite rocks, *Geophys. J. Int.*, *185*, 609–621, doi:10.1111/j.1365-246X.2011.04978.X.

Nielsen, L., and B. H. Jacobsen (2000), Integrated gravity and wideangle seismic inversion for two-dimensional crustal modelling, *Geophys. J. Int.*, *140*, 222–232.

Nixon, P. H. (1987), *Mantle Xenoliths*, Wiley, Chichester.

Oh, S.-H., and B.-D. Kwon (2001), Geostatistical approach to bayesian inversion of geophysical data: Markov chain Monte Carlo method, *Earth Planets Space*, *53*, 777–791.

O'Reilly, S. Y., and W. L. Griffin (2006), Imaging global chemical and thermal heterogeneity in the subcontinental lithospheric mantle with garnets and xenoliths: Geophysical implications, *Tectonophysics*, *416*, 289–309, doi:10.1016/j.tecto.2005.11.014.

O'Reilly, S. Y., and W. L. Griffin (1996), 4-D lithospheric mapping: A review of the methodology with examples, *Tectonophysics*, *262*, 3–18.

O'Reilly, S. Y., and W. L. Griffin (2012), Mantle metasomatism, in *Metasomatism and the Chemical Transformation of Rock*, Springer, Berlin, in press.

O'Reilly, S. Y., J. C. Afonso, W. L. Griffin, and S. van der Lee (eds.) (2010), *The Lithosphere/Asthenosphere Boundary: Nature, Formation, and Evolution*, vii-viii, Lithos Special Issue, *Lithos*, vol. 120, doi: 10.1016/j.lithos.2010.09.017.

Pearson, D. G., and N. Wittig (2008), Formation of Archaean continental lithosphere and its diamonds: The root of the problem, *J. Geol. Soc. London*, *165*, 895–914, doi:10.1144/0016-76492008-003.

Pearson, D. G., D. Canil, and S. B. Shirey (2004), Mantle samples included in volcanic rocks: Xenoliths and diamonds, in *The Mantle and Core*, edited by R. W. Carlson, H. D. Holland, and K. K. Turkeian, Treatise on Geochemistry, vol. 2, Elsevier-Pergamon, Oxford.

Perkins, D., III, and R. C. Newton (1980), The composition of coexisting pyroxenes and garnet in the system CaO- MgO- A1_20_3 -SiO_2 at 900-1,100 C and high pressures, *Contrib. Mineral. Petrol.*, *75*, 291–300.

Petersen, K. D., S. B. Nielsen, O. R. Clausen, R. Stephenson, and T. Gerya (2010), Small-scale mantle convection produces stratigraphic sequences in sedimentary basins, *Science*, *329*(5993), 827–830.

Phillips, R. J., and K. Lambeck (1980), Gravity fields of the terrestrial planets: Long-wavelength anomalies and tectonics, *Rev. Geophys.*, *18* (1), 27–76, doi:10.1029/RG018i001p00027.

Powell, W. G., D. S. Chapman, N. Balling, and A. E. Beck (1988), *Continental heat-flow density*, in *Handbook of Terrestrial Heat-Flow Density Determinations*, edited by Haenel, R. et al., Kluwer Academic Publishers, Dordrecht, 167–222.

Price, D. (ed.) (2009), *Mineral Physics*, Treatise of Geophysics, vol. 2, Elsevier, UK.

Priestley, K. F., and D. P. McKenzie (2006), The thermal structure of the lithosphere from shear wave velocities, *Earth Planet. Sci. Lett.*, *244*, 285–301, doi:10.1016/j.epsl.2006.01.008.

Rawlinson, N., and M. Sambridge (2004), Wavefront evolution in strongly heterogeneous layered media using the fast marching method, *Geophys. J. Int.*, *156*, 631–647, doi:10.1016/j.epsl.2006.01.008.

Rawlinson, N., A. M. Reading, and B. L. N. Kennett (2006), Lithospheric structure of Tasmania from a novel form of teleseismic tomography, *J. Geophys. Res.*, *111*, B02301, doi:10.1029/2005JB003803.

Reigber, C., R. Schmidt, F. Flechtner, R. Konig, U. Meyer, K.-H. Neumayer, P. Schwintzer, and S. Y. Zhu (2005), An Earth gravity field model complete to degree and order 150 from GRACE: EIGEN-GRACE02S, *J. Geodyn.*, *39*(1), 1–10, doi:10.1016/j.jog.2004.07.001.

Ritsema, J., P. Cupillard, B. Tauzin, W. Xu, L. Stixrude, and C. Lithgow-Bertelloni (2009), Joint mineral physics and seismic wave traveltime analysis of upper mantle temperature, *Geology*, *37*, 363–366, doi:10.1130/G25428A.1.

Ritzwoller, M. H., N. M. Shapiro, and S. Zhong (2004), Cooling history of the Pacific lithosphere, *Earth Planet. Sci. Lett.*, *226*, 69–84, doi:10.1016/j.epsl.2004.07.032.

Rousseeuw, P. J., and A. M. Leroy (2003), *Robust Regression and Outlier Detection*, Wiley Series in Probability and Statistics, Wiley and Sons, USA.

Roy, M., J. K. MacCarthy, and J. Selverstone (2005), Upper mantle structure beneath the eastern Colorado Plateau and Rio Grande rift revealed by Bouguer gravity, seismic velocities, and xenolith data, *Geochem. Geophys. Geosys.*, *6*(10), Q10007, doi:10.1029/2005GC001008.

Rubie, D. C., E. Ohtani, and T. S. Duffy (eds.) (2004), *New Developments in High-Pressure Mineral Physics and Applications to the Earth's Interior*, Elsevier, UK.

Rudnick, R. L. (ed.) (2004), *The Crust, Vol 3, Treatise on Geochemistry* (eds, Holland, H.D. and Turkeian, K.K), Elsevier-Pergamon, Oxford.

Rudnick, R. L., and S. Gao (2004), Composition of the continental crust, in *The Crust*, edited by R. L. Rudnick, H. D. Holland, and K. K. Turkeian, Treatise on Geochemistry, vol. 3, Elsevier-Pergamon, Oxford.

Rudnick, R. L., W. F. McDonough, and R. J. O'Connell (1998), Thermal structure, thickness and composition of continental lithosphere, *Chem. Geol.*, *145*, 395–411.

Sandwell, D. T., and W. H. F. Smith (2009), Global marine gravity from retracked Geosat and ERS-1 altimetry: Ridge segmentation

versus spreading rate, *J. Geophys. Res.*, *114*, B01411, doi:10.1029/2008JB006008.

Salisbury, M. H., and D. M. Fountain (1990), *Exposed Cross-sections of the Continental Crust*, 662, Kluwer Acad., Norwell, Mass.

Scales, J. A., and L. Tenorio (2001), Prior information and uncertainty in inverse problems, *Geophysics*, *66*, 389–397.

Schulze, D. J. (1989), Constraints on the abundance of eclogite in the upper mantle, *J. Geophys. Res.*, *94*, 4205–4212.

Schutt, D. L., and C. E. Lesher (2006), Effects of melt depletion on the density and seismic velocity of garnet and spinel lherzolite, *J. Geophys. Res.*, *111*, B05401, doi:10.1029/2003JB002.

Schwalenberg, K., V. Rath, and V. Haak (2002), Sensitivity studies applied to a two-dimensional resistivity model from the Central Andes, *Geophys. J. Int.*, *150*(3), 673–686.

Shapiro, N. M., and M. H. Ritzwoller (2004), Thermodynamic constraints on seismic inversions, *Geophys. J. Int.*, *157*, 1175–1188, doi:10.1111/j.1365-246X.2004.02254.

Shearer, P. (1999), *Introduction to Seismology*, Cambridge University Press, Cambridge.

Shomali, Z. H., R. G. Roberts, L. B. Pedersen, and the TOR working group (2006), Lithospheric structure of the Tornquist Zone resolved by nonlinear P and S teleseismic tomography along the TOR array, *Tectonophysics*, *416*, 133–149, doi:10.1016/j.tecto.2005.11.019.

Simon, N. S. C., R. W. Carlson, D. G. Pearson, and G. R. Davies (2007), The origin and evolution of the Kaapvaal cratonic lithospheric mantle, *J. Petrol.*, *48*, 589–625, doi:10.1093/petrology/egl074.

Simmons, N. A., A. M. Forte, and S. P. Grand (2009), Joint seismic, geodynamic and mineral physical constraints on three-dimensional mantle heterogeneity: Implications for the relative importance of thermal versus compositional heterogeneity, *Geophys J. Int.*, *177*, 1284–1304, doi:10.1111/j.1365-246X.2009.04133.x.

Sobolev, S. V., H. Zeyen, M. Granet, U. Achauer, C. Bauer, F. Werling, R. Altherr, and K. Fuchs (1997), Upper mantle temperatures and lithosphere-astenosphere system beneath the French Massif Central constrained by seismic, gravity, petrologic and thermal observations, *Tectonophysics*, *275*(1-3), 143–164.

Speziale, S., F. Jiang, and T. S. Duffy (2005), Compositional dependence of the elastic wave velocities of mantle minerals: Implications for seismic properties of mantle rocks, in *Earth's Deep Mantle: Structure, Composition, and Evolution*, edited by van der Hilst et al., Geophys. Monograph 160, 301–320. AGU, Washington, D. C.

Stixrude, L., and C. Lithgow-Bertelloni (2011), Thermodynamics of mantle minerals – II. Phase equilibria, *Geophys. J. Int.*, *184*, 1180–1213, doi:10.1111/j.1365-246X.2010.04890.X.

Stracke, A., and B. Bourdon (2009), The importance of melt extraction for tracing mantle heterogeneity, *Geochim. Cosmochim. Acta*, *73*, 218–238, doi:10.1016/j.gca.2008.10.015.

Tarantola, A. (2005), *Inverse Problem Theory and Model Parameter Estimation*, Soc. for Ind. and Appl. Math., Philadelphia.

Taylor, S. R., and S. M. McLennan (1985), *The Continental Crust: Its Composition and Evolution*, Blackwell, Oxford.

Trampert, J., F. Deschamps, J. Resovsky, and D. A. Yuen (2004), Probabilistic tomography maps chemical heterogenities throughout the mantle, *Science*, *306*, 853–856, doi:10.1126/science.1101996.

Turcotte, D. L., and G. Schubert (1982), *Geodynamics: Applications of Continuum Physics to Geological Problems*, John Wiley, New York.

Venables, W. N., and B. D. Ripley (1999), *Modern Applied Statistics with S-PLUS* 3rd ed., Springer-Verlag, New York.

Vilá, M., M. Fernàndez, and I. Jiménez-Munt (2010), Radiogenic heat production variability of some common lithological groups and its significance to lithospheric thermal modeling, *Tectonophysics*, *490*, 152–164 , doi:10.1016/j.tecto.2010.05.003.

Watts, A. B. (2001), *Isostasy and Flexure of the Lithosphere*, Cambridge University Press, Cambridge.

Woodbury, A. D., and G. Ferguson (2006), Ground surface paleotemperature reconstruction using information measures and empirical Bayes, *Geophys. Res. Lett.*, *33*, L06702, doi:10.1029/2005GL025243.

Xu, W., C. Lithgow-Bertelloni, L. Stixrude, and J. Ritsema (2008), The effect of bulk composition and temperature on mantle seismic structure, *Earth Planet. Sci. Lett.*, *275*, 70–79, doi:10.1016/j.epsl.2008.08.012.

Xu, Y., B. T. Poe, T. J. Shankland, and D. C. Rubie (1998), Electrical conductivity of olivine, wadsleyite, and ringwoodite under upper-mantle conditions, *Science*, *280*, 1415–1418.

Xu, Y., T. J. Shankland, and B. T. Poe (2000), Laboratory-based electrical conductivity in the Earth's mantle, *J. Geophys. Res.*, *105*(B12), 27,865–27,875, doi:10.1029/2000JB900299.

Yang, Y., and D. W. Forsyth (2006), Regional tomographic inversion of amplitude and phase of Rayleigh waves with 2-D sensitivity kernels, *Geophys. J. Int.*, *166*, 1148–1160, doi:10.1111/j.1365-246X.2006.02972.x.

Yang, Y., M. H. Ritzwoller, F.-C. Lin, M. P. Moschetti, and N. M. Shapiro (2008), Structure of the crust and uppermost mantle beneath the western United States revealed by ambient noise and earthquake tomography, *J. Geophys. Res.*, *113*, B12310, doi:10.1029/2008JB005833.

Yoshino, T. (2010), Laboratory electrical conductivity measurement of mantle minerals, *Surv. Geophys.*, *31*, 163–206, doi:10.1007/s10712-009-9084-0.

Zeyen, H., and M. Fernàndez (1994), Integrated lithospheric modeling combining thermal, gravity, and local isostasy analysis: Application to the NE Spanish Geotransect, *J. Geophys. Res.*, *99*(B9), 18,089–18,102, doi:10.1029/94JB00898.

Zeyen, H., P. Ayarza, M. Fernàndez, and A. Rimi (2005), Lithospheric structure under the western African-European plate boundary: A transect across the Atlas Mountains and the Gulf of Cadiz, *Tectonics*, *24*, TC2001, doi:10.1029/2004TC001639.

Zhong, S. (1997), Dynamics of crustal compensation and its influences on crustal isostasy, *J. Geophys. Res.*, *102*, 15,287–15,299